ELSEVIER

Contents lists available at ScienceDirect

## Earth and Planetary Science Letters

journal homepage: www.elsevier.com/locate/epsl





# From eons to epochs: multifractal geological time and the compound multifractal - Poisson process

Shaun Lovejoy <sup>a,\*</sup> , Andrej Spiridonov <sup>b</sup>, Rhisiart Davies <sup>a</sup> , Raphael Hebert <sup>c</sup> , Fabrice Lambert <sup>d</sup>

- <sup>a</sup> Physics, McGill University, 3600 University St., Montreal, Quebec, H2A 3T8, Canada
- b Department of Geology and Mineralogy, Faculty of Chemistry and Geosciences, Vilnius University, M. K. Čiurlionio g. 21/27, Vilnius 03101, Lithuania
- Alfred-Wegener Institute Helmholtz Centre for Polar and Marine Research, Telegrafenberg A45, 14473 Potsdam, Germany
- d Geography Institute, Pontificia Universidad Catolica de Chile, Vicuña Mackenna 4860, Santiago, Chile

## ARTICLE INFO

## Edited by Dr H Bao

Keywords: Geological time scale Geochronology Biostratigraphy Scaling Fractals Multifractals

## ABSTRACT

Geological time is punctuated by events that define biostrata and the Geological Time Scale's (GTS) hierarchy of eons, eras, periods, epochs, ages. Paleotemperatures and macroevolution rates, have already indicated that the range  $\approx 1$  Myr to (at least) several hundred Myrs is a scaling (hence hierarchical) "megaclimate" regime. We apply analysis techniques including Haar fluctuations, structure functions, trace moment and extended self-similarity to the temporal density of the boundary events ( $\rho(t)$ ) of two global and four zonal series. We show that  $\rho(t)$  itself is a new paleoindicator and we determine the fundamental multifractal exponents characterizing the mean fluctuations, the intermittency and the degree of multifractality. The strong intermittency allows us to show that the (largest) megaclimate scale is at least  $\approx 0.5$  Gyr.

We find that the tail of the probability distribution of the intervals ("gaps") between boundaries is also scaling with an exponent  $q_D \approx 3.3$  indicating huge variability with occasional very large gaps such that it's third order statistical moment barely converges. The scaling in time implies that record incompleteness increases with its resolution (the "Resolution Sadler effect"), while scaling in probability space implies that incompleteness increases with sample length (the "Length Sadler effect").

The density description of event boundaries is only a useful characterization over time intervals long enough for there to be typically one or more events. In order to model the full range of scales and densities, we introduce a compound multifractal - Poisson process in which the subordinating multifractal process determines the probability of a Poisson event and that this new process is close to the observed statistics.

Scaling changes our understanding of life and the planet and it is needed for unbiasing many statistical paleobiological and geological analyses, including unbiasing spectral analysis of the bulk of geodata that are derived from paleoclimatic and paleoenvironmental archives.

## 1. Introduction

The structure of time scales influences our understanding of the Earth system and biotal evolutionary processes at all time scales. Over billions of years, life and the environment have interacted nonlinearly, and complex bio-geo-processes have led to the formation of the familiar deep-time bio- chemo- litho- and chrono- stratigraphical subdivisions in the International Geological Time Scale (GTS), whose geochronologic time units are the familiar eons, eras, periods, epochs and ages. Their hierarchical nature seems obvious, but how can it be quantified?

Nonlinear systems with variability over wide scale ranges are typically scaling (and hence hierarchical) so that over wide scale ranges, big and small, fast and slow processes are related in a power law manner: fluctuations are qualitatively the same (for reviews see (Lovejoy and Schertzer, 2013), (Lovejoy, 2023)). Scaling analyses of temperature timeseries and its proxies define five scaling ranges: the "megaclimate" down to  $\approx 1$  Myr, "macroclimate" down to  $\approx$  several 100 kyrs, the "climate" down to several kyrs or centuries (in the industrial epoch, decades (Lovejoy, 2013)), "macroweather" down to  $\approx 10$  days, and "weather" down to dissipation scales ( $\approx$  milliseconds), (Lovejoy, 2013),

E-mail address: lovejoy@physics.mcgill.ca (S. Lovejoy).

<sup>\*</sup> Corresponding author.

## (Lovejoy, 2015), (Spiridonov and Lovejoy, 2022).

To date, evidence for the megaclimate comes from marine sediment paleoclimatic archives (Lovejoy, 2015), continental fragmentation, geographical range dynamics (Spiridonov et al., 2022), genus origination, and extinction rates (Spiridonov and Lovejoy, 2022), (Lovejoy and Spiridonov, 2024). These scaling regimes and their transition scales include the scaling nonlinear interactions of the (internal) atmosphere, hydrosphere, and biosphere processes with (external) astronomical and tectonic forcings (Spiridonov and Lovejoy, 2022).

To clarify and quantify the hierarchical nature of bio - geo processes, we recognize multidecadal advancements and steady growth of new quantitative biostratigraphical approaches, which help synchronize proxies of geodynamic, biological, archeological and geochemical processes across the whole range of records (Crampton et al., 2016; Fan et al., 2020; Sadler, 2004; Sadler et al., 2014). Tools such as graphic correlation (Edwards, 1984; 1989; Shaw, 1964) or CONOP (CONstrained OPtimization) techniques (Sadler et al., 2003) help to resolve local and regional inconsistencies in first and last appearances (FADs and LADs) of taxa, and can yield time scales with much higher resolution than traditional zonal time scales. Time resolution achieved in such ordered, resolved and scaled "absolute" time sequences can approach hundreds to even tens of kyrs — thus bringing one to two orders of magnitude improvement in resolution and evenness in time binning of evolutionary sequences (Crampton et al., 2018; Sadler et al., 2003). When the sediment records show relative completeness, the astrochronological approaches can also improve both the accuracy and resolution of time scales, and achieve stratigraphic correlational resolution up to hundreds of kyrs or less, with long eccentricity ( $\approx$  405 kyr) Milankovitch cycles ensuring metronomical evenness of correlated time intervals (Hinnov, 2018; Hinnov and Ogg, 2007; Lieberman and Melott, 2013; Radzevičius et al., 2014; Spiridonov et al., 2020b). Moreover any kind of quantitative or categorical ordered data time series can be correlated to almost arbitrary resolution using cross-recurrence plots and synchronization techniques applied to them (Marwan et al., 2002; Spiridonov et al., 2020a). The commensurability limits the applicability of the cross-recurrence synchronization technique for such high resolution correlation. For example if the patterns of conodont abundance are used for the correlation, all sections should have sufficient conodont fossil record spanning through their depth/height/length (Spiridonov, 2017; Spiridonov et al., 2016).

Despite all such advances in high-resolution correlation, a significant portion of studies, especially generalizing heterogenous multitaxic, multiproxy records across environments and geographic regions or at the global scale, use more conservative time binning schemes, such as GTS2020, or PaleoDB stages (which are related to the international stages), or regional or global zonal scales (Bapst et al., 2012; Daumantas and Spirido, 2024; Fenton et al., 2016; Foote, 2023). The use of international geochronological units is often born out of necessity of the use of the most consistent and most compatible between-studies time bins. When large and heterogenous data sources are aggregated, some data may lack the same time markers (geochemical time series or zonal taxa) and other data (such as mammalian fossils collected in pits) often lack superpositional information (Puolamäki et al., 2006) and so on. Therefore, the GTS and zonal time scales most probably will still be a major reference of geological time in studies aggregating global to regional data in the foreseeable future.

In this study, we quantify the long timescale (>1 Myrs) hierarchy by analyzing the number of stratigraphic boundaries per unit time from two global (including the GTS) and four zonal biostratigraphy series of the Phanerozoic. The scaling of the number of stratigraphic boundaries per unit time - event temporal densities - constitute new paleoindicators whose fluctuation statistics we quantify over scales up to hundreds of millions of years. Using intermittency analysis and extrapolation, we estimate the megaclimate outer scale to be at least of the order of the length of the Phanerozoic Eon and we propose a simple compound multifractal - Poisson model to explain all the observed statistics. In the

model, the probability per time of an event boundary is determined by a (scaling) multifractal process that itself subordinates a Poisson process that then determines the number of boundaries in any interval. Overall, these findings quantify both event gaps and (the opposite) event "clustering" and unless corrected, will bias our statistical analyses (such as spectra and their exponents) and therefore bias our interpretations and understanding of deep time bio-geo-processes. The necessary techniques for correcting such statistical biases will be discussed elsewhere.

## 2. Multifractal boundary densities

## 2.1. The boundaries used in this study

The understanding of the structure of empirical geochronological time scales is fundamental in interpreting all patterns measured against them. Geological time scales, including GTS2020 are defined by the most extreme events, which are usually concentrated at the boundaries of subdivisions: e.g. the P-Tr, J-Tr, and K-Pg boundaries coincide with three of the "Big Five" mass extinctions (Raup and Sepkoski, 1982). Association of biostratigraphy-based geochronological boundaries with the most extreme perturbations is implied by the overwhelming support for the pulsed turnover model of Phanerozoic extinctions and originations (Foote, 2005). Biostratigraphy-based time scales mark the time record of the right tails of geobiological turnovers, thus giving us mechanistic insights on the quantitative nature of statistical laws governing boundary-generating dynamics. Therefore, even if new and much better approaches for global synchronization of various geological records arrive, the understanding of time-scaling properties of geological time scales, gives us direct insights on the saturation of variability, and therefore the time scales needed for statistical characterization of geobiological processes.

Concentrating on the more fundamental boundaries, we limited our study to the Phanerozoic eon and chose the global strata defined by the International Commission on Stratigraphy: the global Geological Time Scale (GTS2020) whose boundary ages are based on (Gradstein, 2020). In addition to the GTS and also at global spatial scales, we analyzed Sepkoski's sub-stage boundaries that define the stratigraphic ranges for marine animal genera (Sepkoski, 2002). To extend the study to series at higher temporal resolutions (but that are still highly significant), we also analyzed four zonal timescales defined by index taxa: Conodonts, Ammonoids, Graptolites and Calcareous nanoplankton. International graptolite zones were taken from the "Silurian" and "Ordovician" chapters (Goldman et al., 2020; Melchin et al., 2020). Since conodonts had time-varying provinciality (as well as some other zonal groups) in order to be consistent we chose European-centric zonation schemes which are the most developed. In the Ordovician conodont zonal compilation was composed of Baltic zones, in the Silurian-Permian global zones, and in the Triassic - Tethyan zones (Aretz et al., 2020; Becker et al., 2020; Goldman et al., 2020; Henderson et al., 2020; Melchin et al., 2012; Ogg et al., 2020). In the case of Devonian ammonoids, global zones were employed; during the Carboniferous, European zones were used, while Tethyan zones were applied from the Permian to the Early Cretaceous, and Western Interior Seaway zones during the Late Cretaceous—thus minimizing spatial discrepancies across time periods and taxonomic groups in zonation (Aretz et al., 2020; Becker et al., 2020; Gale et al., 2020; Henderson et al., 2020; Hesselbo et al., 2020; Ogg et al., 2020). In the case of nannoplankton zones, in the Jurassic Period – Tethyan zones were used, while in the Cretaceous to Neogene global zones were compiled (Gale et al., 2020; Hesselbo et al., 2020; Raffi et al., 2020; Speijer et al., 2020).

Table 1 gives more information about these series. In particular, we may note that the boundary densities ( $\rho(t)$ ) have means  $\overline{\rho}\approx 0.2-0.3$  boundaries/Myr (global) and  $\approx 1$  boundary/Myr (zonal). However as shown in Fig. 1, at 1 Myr resolution,  $\rho(t)$  is highly variable so that these means are inadequate characterizations. In the figure we see that  $\rho(t)$  displays strong temporal variability – intermittent "spikes" - (see also

#### Table 1

Geological timescale characteristics. The resolutions indicated are only nominal. The outer scale  $(\tau_0)$  was estimated from the trace moments (Fig. 3) and are near the graphical value  $10^3$  Myrs = 1 Gyr indicated in Fig. 2 (middle), the multifractal index  $\alpha$  converges to the range 1.2-1.5 (Fig. 2, bottom), and  $H \approx -0.15$  (Fig. 2 top). The mean megaclimate start date is the sum of the estimated duration  $(\tau_0)$  plus the start date of the series. The overall average is  $780\pm280$  Myrs BP. The Sepkoski series is obtained from a database of stratigraphic ranges for marine animal genera (Sepkoski, 2002). References for the Geotimescales (GTS) and the last four (zonal) series are (Peng et al., 2020).

| Series                  | Resolution<br>(nominal) | Start date<br>(Myrs BP) | Duration | Number of boundaries | Number/Myr $\overline{ ho}$ | $Log_{10}\tau_o$ (Myrs) | Megaclimate start<br>(Myrs BP) |
|-------------------------|-------------------------|-------------------------|----------|----------------------|-----------------------------|-------------------------|--------------------------------|
| Geotimescales (GTS2020) | 500 kyr                 | 0                       | 541 Myrs | 103                  | 0.190                       | $2.99{\pm}0.26$         | 980                            |
| Sepkoski sub-stages     | 50 kyr                  | 1                       | 535 Myrs | 154                  | 0.287                       | $2.79 \pm 0.22$         | 620                            |
| Conodont                | 10 kyr                  | 201                     | 286 Myrs | 252                  | 1.13                        | $2.58{\pm}0.28$         | 580                            |
| Ammonoid                | 100kyrs                 | 68                      | 351 Myrs | 330                  | 1.06                        | $3.07{\pm}0.56$         | 1240                           |
| Calcareous              | 10kyr                   | 3                       | 199 Myrs | 203                  | 0.98                        | $2.88{\pm}0.53$         | 760                            |
| Graptolite              | 10 kyr                  | 421                     | 66 Myrs  | 64                   | 1.02                        | $1.87 {\pm} 0.22$       | 500                            |

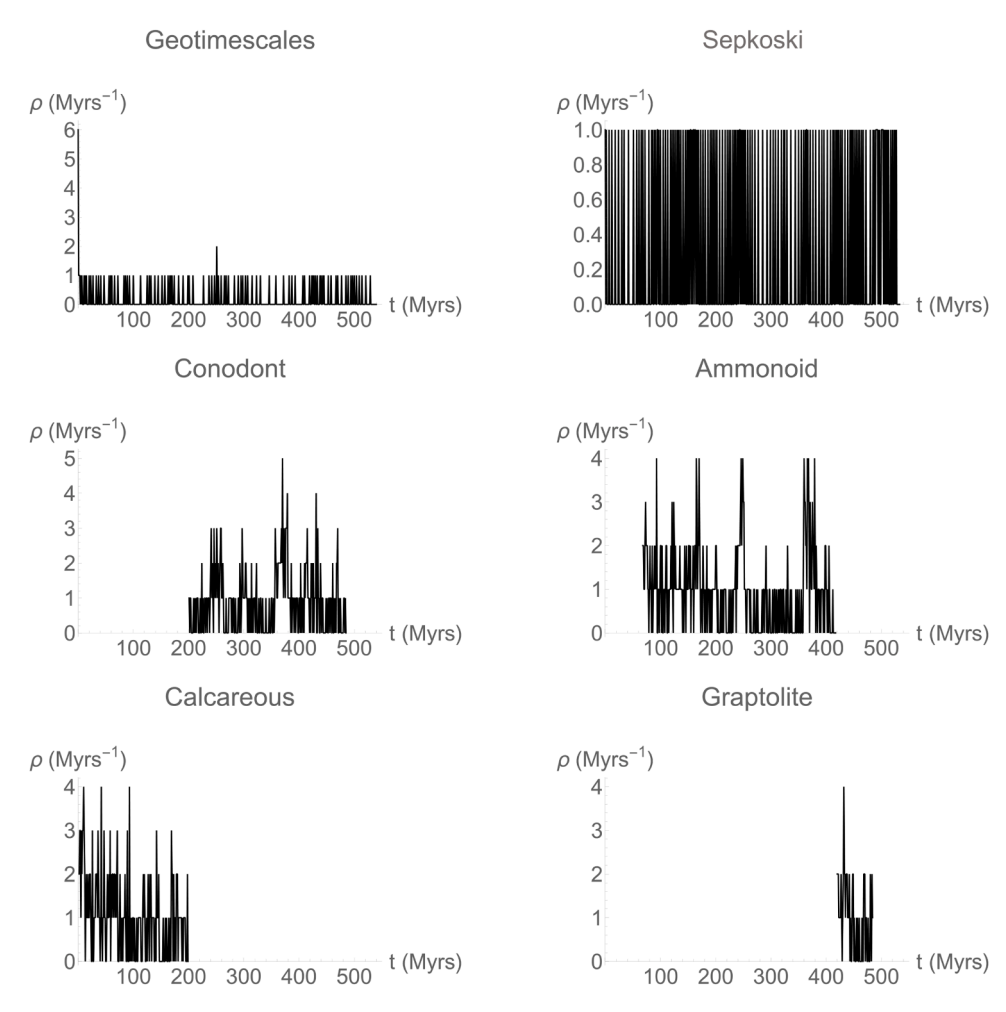


Fig. 1. Temporal boundary densities ( $\rho(t)$ ). The two global chronostratigraphic boundary datasets (top), and biostratigraphic boundaries of conodont, ammonoid, calcareous nanoplankton and graptolite zonal time scales (middle, bottom) in numbers per Myr. Time runs from present to past (see Table B1). Although difficult to see, the upper left ("Geotimescales", GTS2020) has six boundaries in the most recent Myr. "Sepkoski" has more boundaries, but each was separated by at least 1 Myr, it is still binary at this resolution (see also Fig. B1). The figures were produced by dividing the time axis into intervals of fixed length equal to the nominal resolutions (Table B1) and then filling the resulting grids with 1's or 0's depending on whether or not a boundary occurred in the interval. The resulting  $\rho(t)$  series was then degraded (averaged) to 1 Myr. Compare the top right with the simulations in fig. C1.

Fig. B1 and for simulations, appendix C). In addition, the low  $\rho(t)$  regions are associated with "gaps" that turn out to have highly non-Gaussian, "fat tailed" (power law) probability distributions (Section 3.3).

## 2.2. Fluctuations and scaling

The GTS2020 and Sepkoski substages (Fig. 1, top row) are still mostly binary indicator functions (left) or completely binary (right); if

scaling, these are of fractal sets cutoff at a small scale. However, at 1 Myr, the higher-resolution zonal series (bottom rows) already display significant variability, with  $\rho(t)$  approximating the density of a multifractal measure (Fig. B1). The boundary distribution is the temporal analog of the spatial distribution of meteorological measuring stations, first considered as a geometric fractal set of points (Lovejoy et al., 1986), (Korvin et al., 1990; Nicolis, 1993), and later analyzed as the (spatial) density of a multifractal measure,  $\rho(\underline{x})$ , (Tessier et al., 1994). The

theoretical and empirical connections between the two descriptions are discussed in Appendix B (see Fig. B2), and the Compound Multifractal - Poisson Process (CMPP) model is discussed in Section 3.4, appendix C.

To determine the limits of the scaling regimes and estimate the relevant exponents, we used Haar fluctuation analysis (Lovejoy and Schertzer, 2012). The Haar fluctuation of  $\rho(t)$  at resolution  $\Delta t$  is simply the difference between the average over the first and second half of the interval:  $\Delta\rho(\Delta t) = \overline{\rho_{[t,t-\Delta t/2]}} - \overline{\rho_{[t-\Delta t/2,t-\Delta t]}}$  (overbars for temporal averages; below we only consider absolute fluctuations). By combining averaging with differencing, Haar fluctuations overcome important limitations of classical fluctuations that involve only differencing or only averaging (Lovejoy and Schertzer, 2012), they can be easily estimated from irregular chronologies (Lovejoy, 2015).

In scaling processes, fluctuations can be decomposed as follows:

$$\Delta \rho(\Delta t) = \varphi_{\lambda} \Delta t^{H}; \quad \lambda = \frac{\tau_{o}}{\Delta t}; \quad \Delta t \le \tau_{o}$$
 (1)

where  $\Delta\rho(\Delta t)$  is the absolute fluctuation at time scale (lag)  $\Delta t$  and  $\varphi_{\lambda}$  is an intermittent driving stochastic process at scale ratio  $\lambda$  and  $\tau_{0}$  is its outer scale (Schertzer and Lovejoy, 1987; Schertzer et al., 1997), (for reviews (Lovejoy and Schertzer, 2013; Lovejoy, 2023). We assume that  $\varphi_{\lambda}$  has been normalized by its mean, so that  $\langle \varphi_{\lambda} \rangle = 1$  ("< >" indicates "average") and  $\langle \Delta\rho(\Delta t) \rangle = \Delta t^{H}$ , with H the "fluctuation exponent", which is independent of  $\tau_{0}$ . Because we have a single series/realisation, we averaged over all available disjoint intervals at scale  $\Delta t$  (rather than over a statistical ensemble). When H>0, fluctuations tend to grow with scale and the process appears to "wander", whereas when H<0, successive fluctuations tend to cancel and the process appears to fluctuate around a well-defined value. Familiar examples are Brownian motion (H=1/2) and Gaussian white noise (H=-1/2).

Dividing Eq. (1) by its mean, we obtain  $\varphi_{\lambda} = \Delta \rho(\Delta t)/\langle \Delta \rho(\Delta t) \rangle$ , whose statistics can be characterized via the "moment scaling function" exponent K(q):

$$\langle \varphi_{\lambda}^q \rangle = \lambda^{K(q)}$$
 (2)

K(q) is convex and because the mean  $\langle \varphi_{\lambda} \rangle$  is independent of scale, K(1)=0. At the outer time scale  $\Delta t=\tau_0$ ,  $\lambda=1$ , so that  $\langle \varphi_1^q \rangle=1^{K(q)}=1$ : at this scale  $\varphi_1$  is a non-random "sure" value, and the variability vanishes. Scaling Gaussian processes have K(q)=0; hence, there is no outer scale and they are specified only by H. Fractional Gaussian noise has -1 < H < 0, and fractional Brownian motion has 0 < H < 1. Conversely,  $K(q) \neq 0$  implies non-Gaussian processes and intermittent variability that systematically builds up as we move from longer to shorter times. K(q) provides insights into the nature of the variability of geological timescale-defining events, allowing the determination of  $\tau_0$ .

While  $\tau_0$  and H are parameters, K(q) is a convex function that itself needs to be characterized. Fortunately, under fairly general circumstances, K(q) itself can be parameterized by the multifractal index  $\alpha$ (Appendix A) and its derivative at the mean, the intermittency exponent  $C_1 = K'(1)$ .  $C_1$  characterizes how spikiness (sharp transitions) varies with scale and can be directly determined from the function  $F(\Delta t)$  =  $C_1\log (\Delta t/\tau_0)$  (Appendix A). More intuitively,  $C_1$  can be related to the rate at which the ratio of the mean to the root-mean-square fluctuation varies with scale (Appendix A). The final parameter is the multifractal index  $0 < \alpha < 2$  which characterizes the degree of multifractality (Schertzer and Lovejoy, 1987). When H = 0,  $\alpha = 0$  corresponds to a binary monofractal ("off/on") "beta model", and  $\alpha = 2$  to the "lognormal" multifractal. Whereas the  $\alpha=0$  beta model vanishes everywhere except on a fractal set, in contrast, the lognormal has much stronger variability. The name however is bit of a misnomer; where an exact lognormal distribution has logarithms that are normally distributed, a lognormal multifractal has a distribution close to a lognormal except for the very large fluctuations that are (more extreme) power laws (see (Mandelbrot, 1974), (Schertzer and Lovejoy, 1987)).

## 3. Analyses

## 3.1. The multifractal exponents

Using common axes, Fig. 2 provides estimates of  $\langle \Delta \rho(\Delta t) \rangle$  (top) and  $F(\Delta t)$  (middle) whose slopes respectively yield H,  $C_1$ , and (bottom),  $\alpha(\Delta t)$  which are the three "universal multifractal" parameters that specify  $\rho(t)$  (see appendix A for a concise summary of the theory). Each panel shows the results for zonal boundary densities (collectively represented in red) and individual global boundaries (black and gray). In all panels, starting at the left, we note an initial factor  $\approx 3$  - 5 in the scale range over which the statistics transition before converging to scaling regimes at larger  $\Delta t$  (see appendix C). This convergence from effectively a binary (geometric set) description at small  $\Delta t$  to a multifractal description at larger  $\Delta t$  is confirmed in the bottom panel, where at small  $\Delta t$ ,  $\alpha \approx 0$  corresponding to the binary beta model limiting case and then increases with  $\Delta t$  over the transition range to typical scaling range values of  $\alpha \approx 1.2$  – 1.5. Interestingly, in the structure function (top panel), the transition ranges have logarithmic slopes close to the Gaussian value H = -0.5 (dotted). At larger  $\Delta t$ , we see a scaling regime with  $H \approx -0.15$  (top) that extends to the largest scales available ( $\approx 300$ Myrs for the longer, global series), H < 0 implies that successive variations in  $\rho(t)$  tend to cancel out, displaying converging, "stable" behavior. Indeed, and perhaps unsurprisingly, this is close to the (even more stable) value H = -0.25 found for both genus-level extinction and

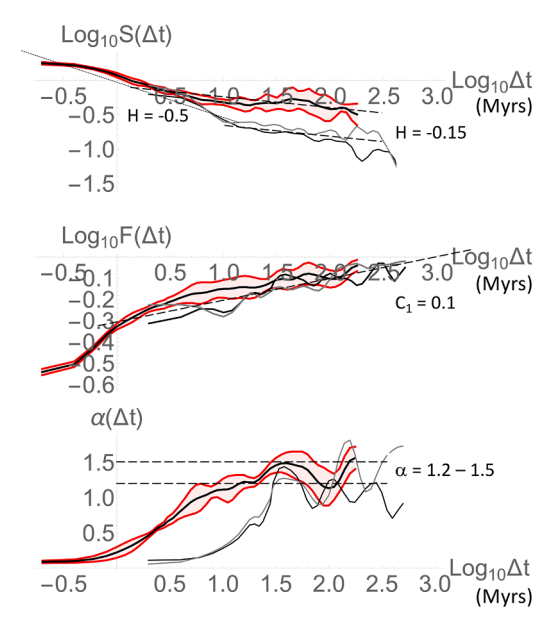


Fig. 2. Scaling and universal multifractal parameters H,  $C_1$ ,  $\alpha$ . Top: First-order structure function  $S(\Delta t) = \langle \Delta \rho \; (\Delta t) \rangle$  as a function of  $\Delta t$  in Myrs; its logarithmic slope is H. The red zone, whose mean is black and width (one standard deviation limits, red) represents the four zonal time scales with  $\rho(t)$  at 100kyr resolution. The thin black and grey lines are the GTS2020 and Sepkoski global boundaries, respectively, at a resolution of 1 Myr. The zonal S0 was multiplied by 10 for clarity. The reference slopes are S10 (dashed, right). S20 has units of number/Myr. S3 and S4 in the middle and bottom panels, respectively, are dimensionless. Compare to the simulations, fig. C2.

*Middle:* The function  $F(\Delta t) = (\Delta t/\tau)^{Cl}$  (Methods), whose logarithmic slope is the intermittency exponent  $C_1$ . The dashed reference line has a slope of  $C_1 = 0.1$ , which represents a rough fit. The line crosses the horizontal axis at the outer scale  $\tau_0$  of the scaling regime ( $\approx 1$  Gyr).

*Bottom:* The third multifractal parameter, the multifractal index  $\alpha$ , estimated at each lag (Methods). At small  $\Delta t$ ,  $\alpha \approx 0$  corresponding to a monofractal (the indicator function of a fractal set), after a range of factor  $\approx 10$ ,  $\rho(t)$  has roughly converged to a multifractal measure with  $\alpha$  roughly in the indicated range. Compare this figure with the simulations fig. C2.

origination rates (Spiridonov and Lovejoy, 2022). At the global scale of analysis, geological timescales reflect the scaling symmetries of key macroevolutionary variables. This strengthens the argument that there is a direct connection between all types of geobiological processes forming a single long-timescale (>1 Myr) scaling dynamic regime.

For the intermittency exponent ( $C_1$ , middle panel), for all series,  $F(\Delta t)$  is roughly scaling for  $\Delta t \geq 3$  Myrs with slope  $C_1 \approx 0.1$ . Significantly, the scaling of  $F(\Delta t)$  not only continues to the largest directly observable  $\Delta t$ , but when extrapolated (dashed line), provides a direct estimate of the outer scale of the variability:  $\tau\approx 1$  Gyr. The dominant contribution to the mean of  $\rho(t)$  comes from a sparse, fractal set of boundaries with fractal dimension 1 -  $C_1$  (so that  $C_1 = 0$  is the nonfractal, uniformly distributed limit). Although  $C_1$  may seem small, since it is an exponent, the implied intermittency increases as the scale range ( $\lambda$ ) increases. Here,  $C_1$ ,  $\alpha$  are close to those in the turbulent (weather regime) wind and temperature fields (e.g. (Lovejoy, 2018)). While in the weather regime  $\lambda$  may be as large as one billion (10 days / 1 millisecond), in the megaclimate, it might not exceed one thousand (1 Gyr/1 Myr). Intermittency is also important for the spectrum,  $E(\omega) \approx \omega^{-\beta}$ , with  $\beta = 1 + 2H$ - K(2), frequency  $\omega$ . Using  $C_1 = 0.1$  and  $\alpha = 1.5$ , we obtain  $K(2) \approx 0.17$ (eqs. A3, A4), and using H = -0.15, we find  $\beta \approx 0.53$ . Without the K(2) "intermittency correction" (e.g. for Gaussian processes),  $\beta=1+2H\approx 0.7$ 

## 3.2. The megaclimate outer scale

Fig. 3 plots  $\log \langle \varphi_{\lambda}^q \rangle = K(q) \log(\tau_o / \Delta t)$ , (Eq. (2)) for  $q=0.1, 0.3, \ldots$  1.9, yielding slopes K(q) and the outer scale  $\tau_o$  (the point of convergence). The figure visually displays how the multifractal variability of  $\phi_{\lambda}$  builds up (from right to left) to smaller scales in a multiplicative cascading manner (Schertzer and Lovejoy, 1987). Table 1 shows  $\tau_o$  estimates; the (logarithmic) mean for all six series is  $\log_{10}\tau_o=2.83\pm0.44$  ( $\approx 680$  Myrs), in accordance with the  $F(\Delta t)$  analysis (Fig. 2 middle) that found  $\log_{10}\tau_o\approx 3$  (i.e., 1 Gyr). Because  $\tau_o$  is estimated by extrapolation, the uncertainties (indicated by arrows) are fairly large.  $\tau_o$  is an estimate of the limiting megaclimate time scale, the longest time over which variability in  $\rho(t)$  builds up. However, it is possible that megaclimate bio-geo processes only hold over the more recent  $\approx 1$  Gyr, and that this "start date", might limit the scaling ranges of the older samples. Some evidence for this can be seen in Table 1, where the two oldest series (Conodont and Graptolite) also have the smallest  $\tau_o$  values. It should be

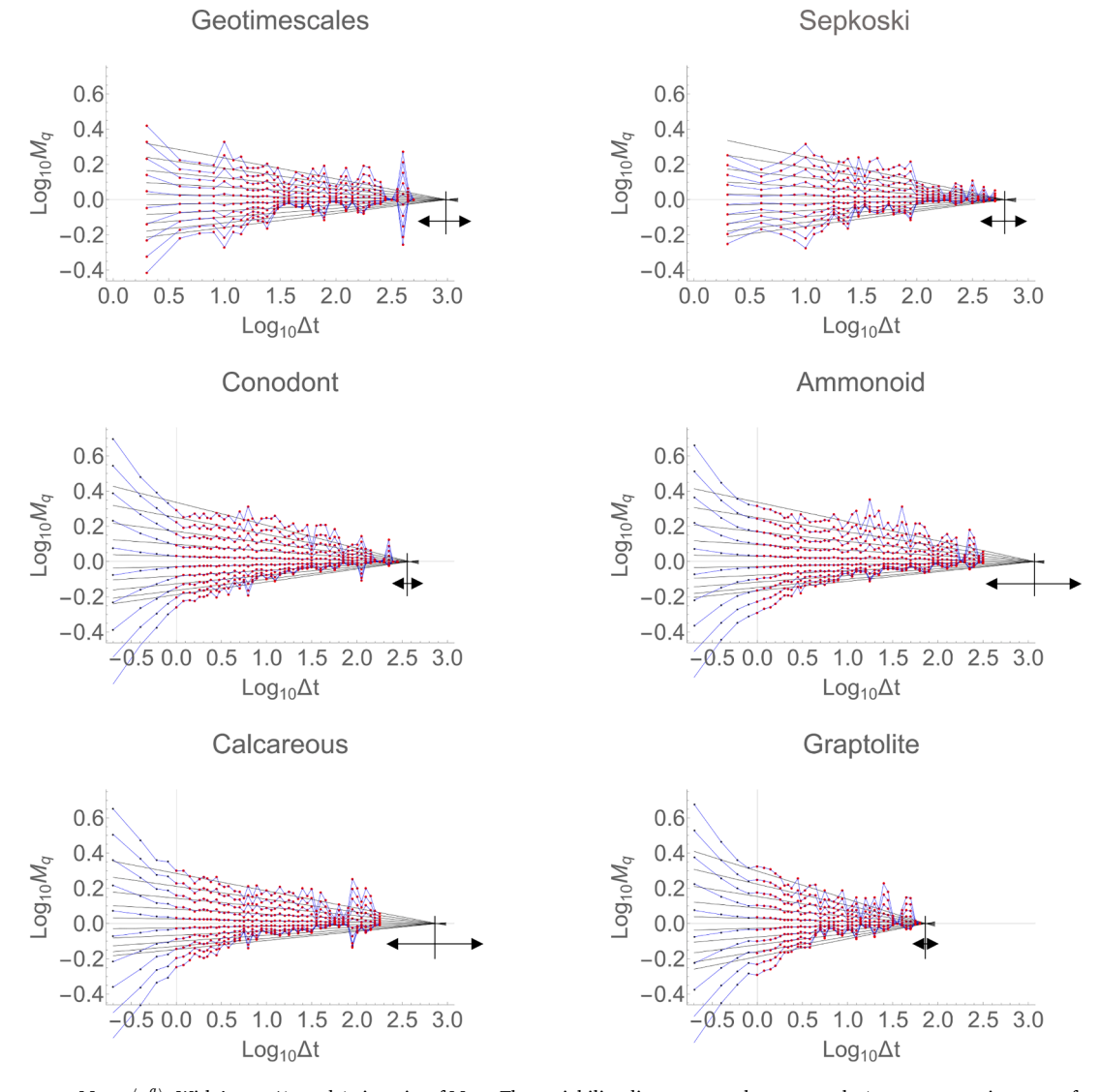


Fig. 3. Trace moments  $M_q = \langle \varphi_\lambda^q \rangle$ . With  $\lambda = \tau_o/\Delta t$  and  $\Delta t$  in units of Myrs. The variability disappears at the outer scale  $\Delta t = \tau_o$ ; regressions were forced through this common point (Table 1). The blue points with  $\Delta t < 1$  Myr were excluded from the regressions because they were in the transition zone discussed above. Haar fluctuations require at least two data points for their estimation; hence, the smallest  $\Delta t$  values are 2 and 0.2 Myrs). The double-headed arrows indicate the 1 standard deviation uncertainty limits. The slopes yield K(q), which is used to estimate  $C_1 = K'(1)$  (Table B1). Compare this figure with the simulations fig. C3.

noted that the Graptolite series covering only two periods (Ordovician and Silurian) is the shortest, with the fewest (64) boundaries. Adding the estimate of  $\tau_o$  to the start date of the series (Table 1) gives the megaclimate transition scale of 780 $\pm 280$  Myrs. We also note that the CMPP model discussed below and in appendix C suggests that we should be cautious about extrapolating beyond the actual length of the series, i.e. the duration of the Phanerozoic, 0.5 Gyrs.

If the outer scale of megaclimate variability extends beyond the Phanerozoic Eon it would suggest that the current eon-style geobiological time variability not only started somewhat before the Phanerozoic proper, but also that it hasn't yet reached its limit, that we haven't "seen" the saturation in a range of possible biogeological and megaclimatic states and that our eon's variability will continue to grow. The outer scale of the Phanerozoic style Earth system dynamics - the "megaclimate" - is suspiciously similar to time scales of "finished" Archaean and Hadean eons, each  $\approx 1.5$  and 2.0 Gyrs in duration. Essentially, this is the time scale where we can see a full range of coupled Earth-Life dynamics unfold. The study of scaling characteristics of other eons are currently limited by the number of globally recognized boundaries, with the Proterozoic being subdivided only into period time scales (tens of Myrs), and the Archean being subdivided only into eras. As the Precambrian stratigraphy matures, these grand subdivisions of geological time will have increased resolution and will provide insights into early Earth scaling regimes that may differ from the Phanerozoic Eon megaclimate. For example, "the Boring Billion" was characterized by quiescence of the evolution of life, climate, and tectonics (Stern, 2023), which could imply much shorter outer scales of middle Proterozoic biogeological variability.

## 3.3. Low $\rho(t)$ : incompleteness and the length and resolution Sadler effects

On the time axis, the biostratigraphic boundaries form geometric sets of points and because they are scaling, they are fractal sets. The precise relationship between fractal dimensions of the geometric set of boundary points and the multifractal density exponent K(q) is discussed in Appendix B. When  $\rho(t)$  is large, there are sufficient points to estimate it reliably; however, when  $\rho(t)$  is low, it is poorly estimated. In addition, because the time interval between boundaries is  $\approx 1/\rho(t)$ , long intervals (big "gaps") occur when  $\rho(t)$  is low. Therefore, to study gaps, it is better to return to the set description. Interestingly, as shown by the theory and numerics (appendix C), both high and low  $\rho(t)$  regions are realistically modelled in the CMPP and the model exhibits both Sadler effects, but the full theory has yet to be developed.

An alternative analysis method that clearly demonstrates the scaling of the low density intervals is to directly study the scaling of the probability distribution of intervals between successive boundaries:  $(\tau(n),$  Fig. 4). Fig. 5 shows the probability  $\Pr(\tau' > \tau)$  of a randomly chosen interval  $\tau'$  exceeding a fixed interval  $\tau$  (i.e. 1 minus the (usual) Cumulative Distribution Function, CDF). Plotted on a log-log plot, we see that the extreme probability "tails" are "fat" i.e. they decay algebraically in a

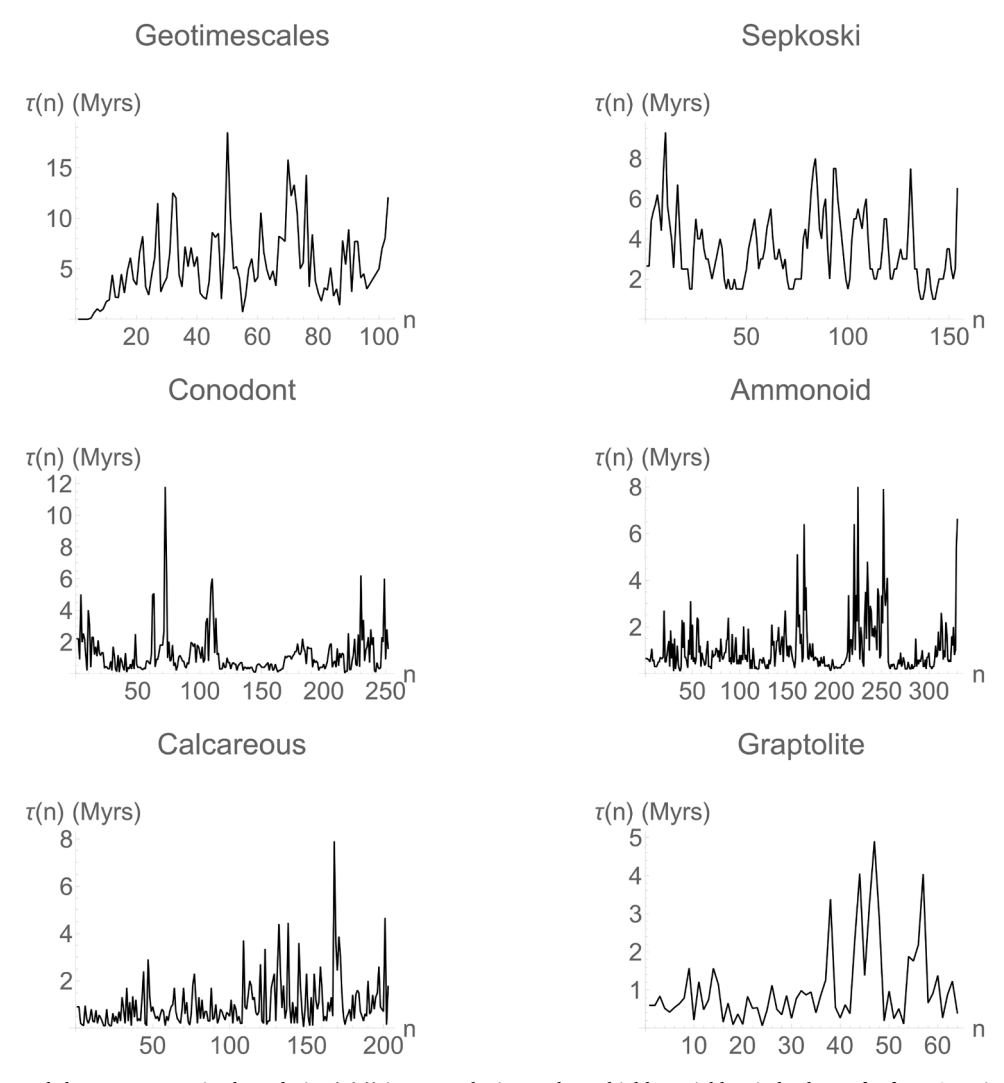
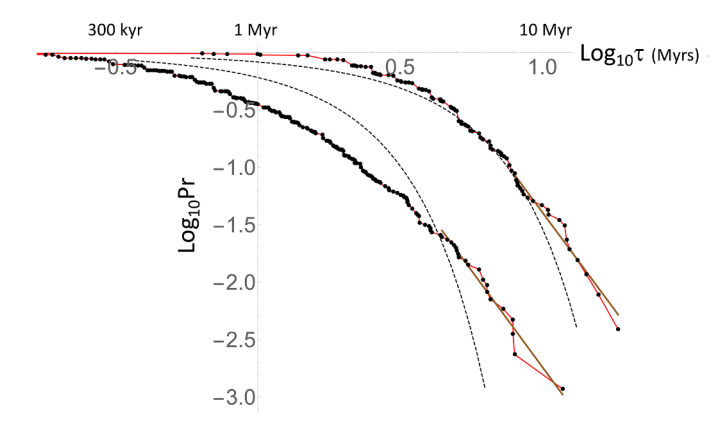


Fig. 4. The  $n^{th}$  time intervals between successive boundaries ( $\tau(n)$ ) in Myrs. The intervals are highly variable – indeed very far from Gaussian. This is quantitatively established in the probability analysis given in Fig. 5. Compare this figure with the simulations fig. C4.



**Fig. 5.** Probability distributions  $\text{Pr}(\tau'>\tau)$  for the duration of a randomly chosen inter-boundary interval  $\tau'>$  exceeding a fixed threshold  $\tau$ . The upper right curve is from the pooled GTS and Sepkoski intervals, the left curve is from pooled intervals from the four zonal series. The brown regression lines show absolute slopes ( $q_D$ ) of 3.3, 3.4 respectively (fit to the extreme 20 points in both cases). The dashed curved lines are the best fitting Gaussians. The extreme points correspond to 4.02 and 6.06 standard deviations respectively, hence Gaussian probabilities of  $\approx 6 \times 10^{-5}$  and  $1.3 \times 10^{-9}$  respectively. In comparison, the lowest probability levels available from the data are  $3.8 \times 10^{-3}$  and  $1.1 \times 10^{-3}$  respectively. Even for short intervals, the Gaussian seems to be a poor fit.

Compare this figure with the simulations fig. C5.

power law manner: scaling in probability space:  $\Pr(\tau' > \tau) \approx \tau^{-q_D}$ . To increase the sample size (to better characterize the low probabilities), data were pooled from the two global (right), and the four zonal (left), series yielding regression exponents  $q_D \approx 3.3$  and 3.4 respectively. In the figure, the distributions are compared to the best fitting Gaussians (that have  $q_D = \infty$ ). It is obvious that the distributions are very far from Gaussian with extreme points corresponding to Gaussian probabilities of  $\approx 10^{-6}$ ,  $10^{-9}$  and this, even though the number of points is <1000. Note that statistical moments of order  $q > q_D$  diverge with sample size so, that for example,  $q_D$ <2 implies that the variance is not well defined and  $q_D$ <1, that the mean interval is likewise ill-defined (in practice, this implies that they are sample size dependent). We may note that although the exact distribution of intervals depends on the temporal resolution (see Table 1 for the nominal resolutions), due to the scaling, the exponent  $q_D$  will not depend of the resolution (at least for resolutions corresponding the scaling regime of the interval probabilities).

Due to the normalization of the probabilities, probability distributions cannot be power laws over the entire range of intervals, yet it is nevertheless notable that even at small intervals (high probabilities) that the distribution is not Gaussian. This is in contrast with typical geochronology interval distributions, that often display fairly clear transitions from roughly Gaussian distributions (frequent, small intervals) to power law tails for the (rare) large intervals. Such abrupt transitions allow for an objective separation of short intervals whose (short, roughly Gaussian intervals) are associated with varying sedimentation rates, from the much longer "gaps" that may be associated with missing strata (incomplete records). Such gaps can arise in several ways: lack of host rock strata of the right age, failures of fossil preservation in those strata, or inadequate collection and identification of fossils from those strata.

The (original) Sadler effect refers to the observation (Sadler, 1981) that as one increases the temporal resolution of a series of measurements, that its incompleteness tends to increase, it is a resolution dependent effect. If the measurements form a fractal set on the time axis (see Appendix B and Figs. B1 and B2), then using disjoint boxes of duration L, the number required to "cover" the set of boundaries will be  $\approx L^{-Dbox}$  with box dimension  $D_{box} < D_{time}$ , ( $D_{time} = 1$ , it is the dimension of the time axis). Box counting may be viewed as a way of representing/

approximating the set at finite resolution, here defined by segments of duration L on the time axis. If the measurements were dense on the time axis (i.e. if they were complete at resolution *L*), then the number of boxes covering the unit interval would be  $L^{-Dtime} = L^{-1}$  so that the fraction of boundaries covered by boxes (i.e. the fraction of the record that is complete at resolution *L*) would be  $L^{-Dbox} / L^{-1} = L^{Cbox}$  where  $C_{box} = 1$ - $D_{box} > 0$  is the box codimension.  $C_{box}$  is also an incompleteness exponent since it quantifies that the rate at which the incompleteness increases as the resolution is decreased. See Table B1 for codimensions and Fig. B2 for the box-number scaling for the strata studied here (also shown In Fig. B2 are plots yielding the slightly different correlation fractal codimensions). Alternatively, we can consider the effect of resolution dependence on the boundary density. When H < 0 (as it is here), it governs the resolution dependence of anomaly fluctuations  $\overline{\rho'}_{\tau}$  where the overbar indicates temporal averaging, the subscript the averaging duration. The prime is the anomaly with respect to the long term average  $\rho' = \rho - \overline{\rho}$ . When H < 0,  $\overline{\rho'_{\tau}} \approx \tau^H$  so that H is the exponent that determines the rate at which density anomalies tend to approach the long term average as they are averaged over longer and longer durations.

This basic resolution - dependent Sadler effect thus depends on the underlying temporal scaling. There is however another related scaling effect on measurement incompleteness: the tendency of longer and longer records to be more and more incomplete (if only because longer stratigraphic records are needed to straddle longer gaps). This effect is also a consequence of scaling, but rather in probability space, the power scaling of the tail of the probability distribution of the intervals extreme gaps, (Fig. 5). As shown in (Lovejoy et al., 2025), these power law tails imply that (at fixed temporal resolutions), longer series will tend to have larger gaps and hence to be more incomplete.  $q_D$  is thus the length incompleteness exponent, determining how increasing the series length increases its incompleteness. To distinguish this length effect from the resolution effect, we will refer to the former as the "Length Sadler effect" and to the latter (the original Sadler effect) as the "Resolution Sadler effect", quantified by  $q_D$  and  $C_{box}$  respectively.

A further aspect based on the first principles of sedimentation, erosion and rock cycling, is that all else being equal, older records should be proportionately (exponentially) less complete. This generic feature can induce different kinds of biases in the analysis of the fossil record of past events and trends (e.g. Raup, 1972). This profound question wasn't explicitly studied here and certainly deserves separate attention.

## 3.4. Improving the scaling using extended self similarity

Scaling is a scale invariance symmetry that is only exact on a statistical ensemble, it is almost surely broken on any individual realization (indeed on any finite number of realizations). Therefore, random deviations are almost surely present and it may require a large data set to yield convincing scaling regimes and exponent statistics. In addition, in any physical system, scaling only holds over a finite range of scales and here this range may be as small as a factor of 1000 with - as is the case here - the available data spanning an even smaller range. On the other hand, modern scientific methodology assumes that the simplest (and hence a priori) assumption about a physical system: i.e. that symmetries hold unless specific symmetry breaking processes/ mechanisms can be identified (recall that due to Noether's theorem, symmetries imply conservation laws, here, various exponents are conserved under scale changes).

To support the above interpretation of the small  $\Delta t$  scaling break—as resulting from the relatively small number of boundaries and various finite-resolution effects—and to obtain broader scaling regimes and more accurate exponent estimates, one can leverage the fact that Eq. (2) relates moments of different orders. The simplest way to exploit this is to use the structure functions (Eq. 3) to express the time interval  $\Delta t$  in terms of the mean (q=1) fluctuation:  $\Delta t = \langle \Delta \rho(\Delta t) \rangle^{1/H}$  so that

expressing the  $q^{\text{th}}$  moment in terms of the first, we obtain:  $\log \langle \Delta \rho(\Delta t)^q \rangle = (1-K(q)/H)\log \langle \Delta \rho(\Delta t) \rangle + const$  ("Extended Self-Similarity", ESS (Benzi et al., 1993), Fig. 6). The red points in Fig. 6 (used in the regressions) are from lags  $\Delta t \geq 1$  Myr and show that the scaling (the linearity on a log-log plot) starts roughly at 1 Myr (the black points are for  $\Delta t < 1$  Myr. We see that the transition regime has been largely eliminated, so that the scaling is somewhat better than it appears in Figs. 2 and 3.

## 3.5. The compound multifractal - Poisson process

In the previous section, we noted that even if the underlying processes that generate boundary events are scaling over the whole observed range, empirical statistics will show various finite size effects for time scales shorter than the average inter-event time i.e. below  $\bar{\rho}$ . In Section 3.4, we tried to extend the empirical range of the scaling by using the ESS analysis technique. However, an ultimately more compelling justification of scaling is possible by the construction of a pure scaling model that generates realizations that are statistically indistinguishable from the empirical series of event boundaries. In appendix C we discuss in detail such a model, the Compound Multifractal

Poisson Model (CMPP) in which a (pure scaling) multifractal process does not determine the event directly but rather the *probability* of an event. Once the probability has been specified, a ("subordinated") Poisson process determines the actual occurrence (or nonoccurrence) of an event in any resolution element. Readers are invited to view the figures in appendix C that reproduce the empirical Figs. 1–6 both qualitatively and quantitatively.

## 4. Conclusions

Human life, the rise of civilization, and the evolution of the Earth are punctuated by hierarchically structured events that color our notions of time and its passage. In the Phanerozoic Eon, there are notable stratigraphic boundaries - marked by "golden spikes" - that separate major portions of time and define the Geological Time Scale. Hierarchical processes that act over wide ranges of scales are typically scaling and their variability builds up from large to small and from slow to fast in a multiplicative manner.

Multifractal processes provide a natural framework (Lovejoy and Schertzer, 2013), (Lovejoy, 2023) for studying variability over a wide scale range, and five wide scaling regimes have been identified with the

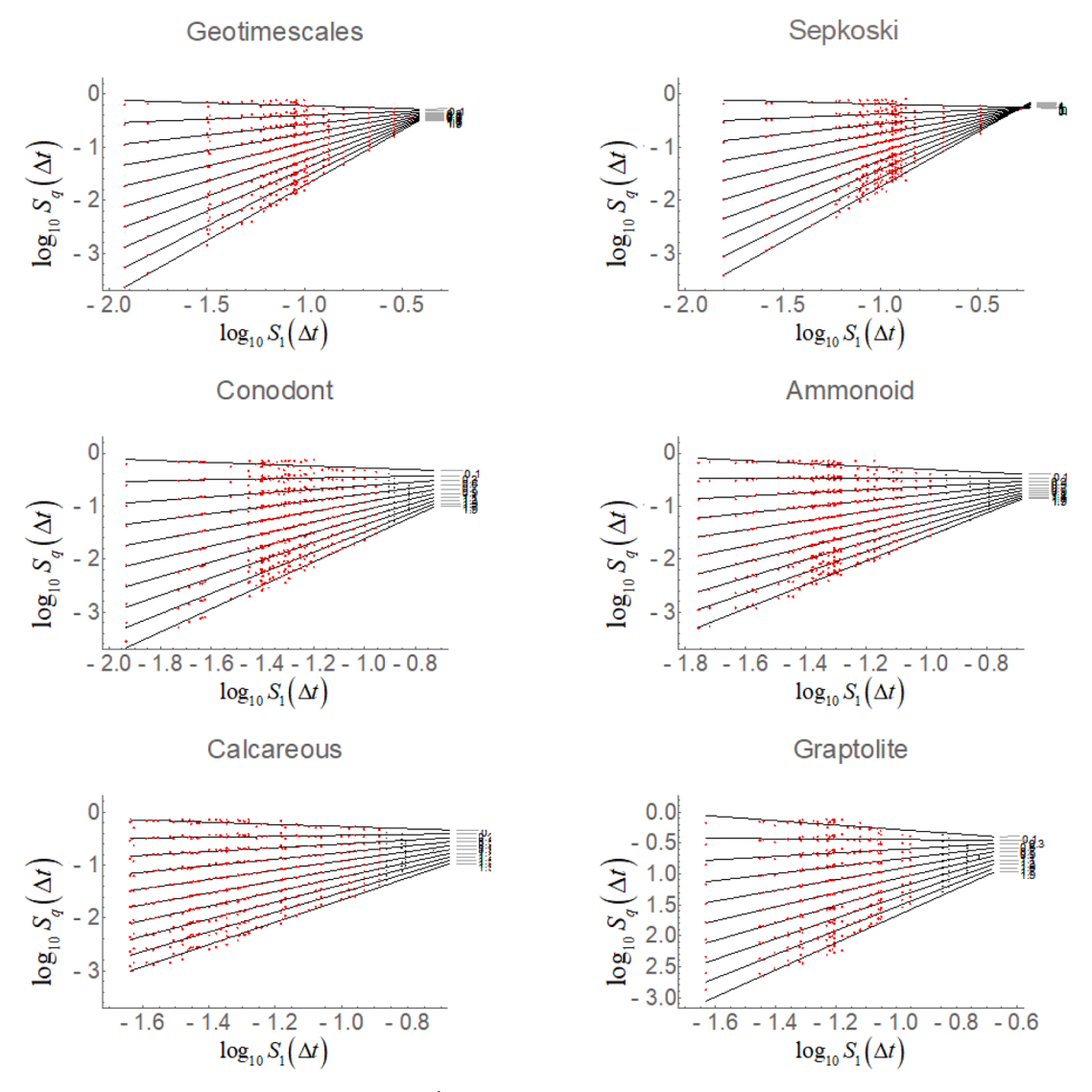


Fig. 6. The extended self-similarity (ESS) plots. The scaling of the  $q^{\text{th}}$  order moments ( $S_q = \log(\Delta \rho(\Delta t)^q)$ ) as functions of the first order moments ( $M_1$ ) for moments order q = 0.1, 0.3, ... 1.9 (top to bottom). The regression slopes (= 1 - K(q)/H) are shown indicating the excellent scaling from  $\Delta t \geq 1$  Myr (red points). The fits are over the red points that correspond to lags ( $\Delta t$ )  $\geq 1$  Myr (the black are for  $\Delta t < 1$  Myr). Compare this figure with the simulations Fig. C6.

megaclimate at the lowest frequencies (Lovejov, 2015). So far, evidence for a megaclimate spanning ~ 1 Myr to (at least) several hundred Myrs has been based on paleotemperatures (Lovejoy, 2015), paleo-sea levels (Lovejoy et al., 2025), continental fragmentation (Spiridonov et al., 2022), geographical range dynamics (Spiridonov et al., 2022) and extinction and origination rates (from the Paleobiology Data base of taxonomic occurrences (Spiridonov and Lovejoy, 2022), (Lovejoy and Spiridonov, 2024). The megaclimate is the expression of complex nonlinear interactions between life and geology, and these determine the events in Earth's history that define stratigraphic boundaries, the hierarchy of eons/eras/periods/epochs/ages. Up until now, the upper limit of the megaclimate variability has not been etimated. By using a new paleoindicator – the boundary density - and intermittency ( $F(\Delta t)$ , Fig. 2) and trace moment analysis (Fig. 3), we have presented evidence that the event density variability in the current Phanerozoic Eon Earth systems dynamics may saturate at time scales  $\tau_o\approx 0.5$  - 1 Ga.

The stratigraphic boundary horizons are fractal sets when they are represented as geometric sets of points on the time axis delimiting global GTS2020 stages or Sepkoski substages boundaries, as well as taxon specific (zonal) boundaries, (Appendix B). If we represent the boundary set on the time axis, then the set at resolution L is defined by the number N(L) of disjoint boxes duration L needed to cover it. Due to the scaling,  $N(L) \approx L^{-Dbox}$  where  $D_{box}$  is fractal box dimension that we estimated (Table B1). In section 2.5, we showed how it implies and quantifies the resolution Sadler effect.

However, fractal sets generally define an infinite hierarchy of exponents and  $D_{box}$  is only one of the family. It is generally more fruitful to consider their densities as the fundamental quantities, here the temporal densities of the boundaries ( $\rho(t)$ , boundaries/Myr). These densities are multifractal functions (more precisely, densities of singular multifractal measures, "generalized functions"). We used Haar fluctuation analysis to analyse  $\rho(t)$  from the global and zonal boundaries, confirming their scaling nature, and quantifying the entire hierarchy with more fundamental exponents  $\alpha$ ,  $C_1$ , H. At small lags ( $\Delta t$ ), there were transition regimes, but for  $\Delta t > \approx 3$  - 5 Myrs, the fluctuations ( $\Delta \rho(\Delta t)$ ) displayed multifractal scaling to their largest scales (for note that for the shortest scales, Figs. 2 and 6 extends the scaling down to  $\Delta t \approx 1$  Myr). The three basic multifractal exponents were estimated as:  $H \approx -0.15$ , (mean fluctuations),  $C_1 \approx 0.1$  (intermittency) and  $\alpha \approx 1.2$  - 1.5 (multifractal index).

By showing that geological time scales (including the inter-boundary time intervals with their occasional "gaps", Fig. 5 that is the basis for the Length Sadler effect) are scaling, we have quantified the long-held idea that biogeological processes are hierarchical, and we have provided further support for the hypothesis of a single megaclimate scaling regime with outer scale at least as long as the records that we examined (0.5 Gyr). Indeed, the boundary density itself has been shown to be a new paleoindicator with implications for geochronologies (Lovejoy et al., 2025).

Finally, we note that the (multifractal) event density description does not represent the short time scales below the average inter-event time  $\bar{\rho}$ . Rather than viewing this a break in the scaling of the underlying bio-geo processes, we developed a Compound Multifractal - Poisson Process model (CMPP) in which a pure scaling process determines the probability of an event – not the direct occurrence (or absence) of an event.

The multifractal "subordinator" subordinates a Poisson process. We show with some theory and numerics (appendix C) that the CMPP reproduces both the low and high density statistics, supporting the hypothesis that the underlying processes are indeed scaling over the scale range observed here.

Not long ago, paleorecords were limited to scores or hundreds of points, enough to identify notable (intermittent) events, but not sufficient to reliably characterize the "background" variability that was (mistakenly) thought to be an uninteresting white noise. Modern, "big" paleorecords have hundreds or thousands of times more points allowing characterization of the background that in fact contains most of the variability and that demands systematic statistical - including spectral – analysis. Yet due to the scaling of geological time, paleorecord geochronologies also turn out to be multifractal with scaling "gaps", and the biases (particularly in spectral and other scalng exponents) that they introduce must be corrected (this includes Lomb-Scargle and Multi Taper spectral techniques (Lovejoy and Spiridonov, 2024), which could have considerable implications in characterizing possible regularity of mass extinctions and other globally significant events.

## **Funding**

S.L. was funded by a National Science and Engineering Research Council (Canada) grant 222858. A.S. was supported by the project S-MIP-24-62 BretEvoGeneralized. F.L. was funded by ANID - Fondecyt 1231682.

## CRediT authorship contribution statement

Shaun Lovejoy: Writing – original draft, Supervision, Software, Methodology, Investigation, Funding acquisition, Formal analysis, Conceptualization. Andrej Spiridonov: Writing – review & editing, Validation, Investigation, Formal analysis, Conceptualization. Rhisiart Davies: Validation, Formal analysis. Raphael Hebert: Writing – review & editing, Conceptualization. Fabrice Lambert: Writing – review & editing, Methodology, Conceptualization.

## **Declaration of competing interest**

The authors declare the following financial interests/personal relationships which may be considered as potential competing interests:

Shaun Lovejoy reports financial support was provided by National Science and Engineering Research Council (Canada). The authors declare that they have no known competing financial interests or personal relationships that could have appeared to influence the work reported in this paper.

## Acknowledgements

We acknowledge the editors of Nature, Science, Nature Geoscience, Proceedings of the National Academy of Sciences, AGU Advances and Physical Review Letters. The work profited from discussions at the Climate Variability Across Scales (CVAS) working group of the Past Global Changes (PAGES) programme.

## Appendix A. Multifractal processes

## A1. Discussion

The zonal and other chronostratigraphic boundaries studied here (see Table 1) can be represented as points on the time axis that separate geostrata. A geometric set of points that is scaling is a fractal set, and it is notably characterized by its fractal dimension. However, a single fractal dimension is generally a rather partial description of its statistics and in addition, many definitions of fractal dimension are possible (see Appendix B). For full statistical characterization, it is best to consider the density of the points on the set. Mathematically, this density is a function (here of time), and if

scaling, it is the density of a singular multifractal measure and requires an exponent for each q, (K(q) in eq. 2), equivalent to an infinite hierarchy of exponents [Hentschel and Procaccia, 1983, Grassberger, 1983, Schertzer and Lovejoy, 1983]. This connection is discussed at length in Appendix B, that includes direct estimates of fractal box dimensions (often used as a surrogate for the Hausdorff dimension) as well of fractal correlation dimensions (Fig. B2, Table B1).

If we take the  $q^{th}$  moments of eq. 1 and use the definition in eq. 2 we can define the  $q^{th}$  order structure function:

$$S_q(\Delta t) = \langle \Delta \rho(\Delta t)^q \rangle = \langle \varphi_{\lambda}^q \rangle \Delta t^{qH} = \tau^{K(q)} \Delta t^{\xi(q)}; \quad \xi(q) = qH - K(q). \tag{3}$$

 $S_q(\Delta t)$  is the mean  $q^{\text{th}}$  order moment of the (absolute) fluctuations, it is characterized by its exponent  $\xi(q)$  and because K(1) = 0, we have  $\xi(1) = H$ . Equivalently, the statistics of  $\rho$  can be characterized by the probability distributions of fluctuations that are also scaling, and whose exponents – the codimension function - may be retrieved from  $\xi(q)$  via Legendre transformation [Parisi and Frisch, 1985].

From eq. 3, we see that in addition to the fluctuation exponent H, we also need to parameterize K(q). Due to the existence of stable, attractive "universal" multifractal processes [Schertzer and Lovejoy, 1987], K(q) is often taken to be of the universal multifractal form:

$$K(q) = \frac{C_1}{\alpha - 1}(q^{\alpha} - q); \quad 0 \le \alpha \le 2; \quad C_1 \ge 0$$
 (4)

K(q) is thus determined by two fundamental parameters: the codimension of the mean  $C_1$ , often called the "intermittency exponent", and the multifractal index  $0 \le \alpha \le 2$ . From this, we can verify that K(1) = 0,  $K'(1) = C_1$ , and  $\alpha = K''(1)/K'(1)$ . A full characterization of the statistics of  $\rho(t)$  over a given scaling regime is then determined by the triplet H,  $C_1$ ,  $\alpha$ .

## A2. The fluctuation exponent H

As outlined above, H characterizes the scaling of the mean (q = 1). When H > 0, fluctuations tend to grow with lag  $\Delta t$  so that the series tends to "wander", and when H < 0, fluctuations decrease with lag, they tend to cancel each other out. When  $0 \le H \le 1$ , fluctuations may be estimated by differences, but here with H < 0, differences are too restrictive, and we use Haar fluctuations (based on the Haar wavelet) useful when -1 < H < 1, which is an adequate range for the vast majority of geoprocesses [Lovejoy and Schertzer, 2012] corresponding roughly to a range of spectral exponents  $-1 < \beta < 3$ .

## A3. The intermittency exponent $C_1$

The role of  $C_1$  is less intuitive; for quasi-Gaussian processes,  $C_1 = 0$ ; hence, K(q) = 0, and only H is important. In this special case, when  $0 \le H \le 1$ , the process is a fractional Brownian motion (with H = 1/2 it is classical Brownian motion), and when -1 < H < 0, the process is fractional Gaussian noise with the special case H = -1/2 corresponding to (usual) Gaussian white noise.  $C_1 > 0$  characterizes the tendency of the series to make jumps and transitions: to be intermittent. For  $\rho(t)$  this implies that there are occasional high density "spikes" that are significantly larger than the mean. The spikes exceeding the mean form a fractal set with codimension  $C_1$  (hence on the d = 1 time axis, a fractal dimension  $1 - C_1$ ). A more intuitive interpretation of  $C_1$  is that it characterizes the rate of divergence of the ratio of the mean to the root mean square (RMS) fluctuation:

$$\frac{\langle \Delta \rho(\Delta t) \rangle}{\langle \Delta \rho(\Delta t)^2 \rangle^{1/2}} = \left(\frac{\Delta t}{\tau}\right)^{aC_1} \tag{5}$$

where (from eq. 4), we find  $a = (2^{\alpha-1}-1)/(\alpha-1)$ . Since  $0 \le \alpha \le 2$ , the constant  $\frac{1}{2} \le a \le 1$  and it depends only weakly on  $\alpha$  (in the above, with,  $\alpha \approx 1.2 - 1.5$  we find  $a \approx 0.74 - 0.83$ ).

## A4. Estimating $C_1$ , $F(\Delta t)$

We define the function  $F(\Delta t)$  as:

$$\log F(\Delta t) = \log \langle \Delta \rho(\Delta t) \rangle - \frac{\langle \Delta \rho(\Delta t) \log \Delta \rho(\Delta t) \rangle}{\langle \Delta \rho(\Delta t) \rangle} \tag{6}$$

F can be obtained either directly from the corresponding moments or by finite differences from the moments of  $\phi_{\lambda}$  [Lovejoy and Schertzer, 2013]. In a scaling regime:

$$F(\Delta t) = \left(\frac{\Delta t}{\tau_0}\right)^{C_1} \tag{7}$$

Plotting  $\log(F(\Delta t))$  against  $\log(\Delta t)$  therefore yields an estimate of  $C_1$  as the slope as well as an estimate of  $\tau_0$  as the intercept with the horizontal axis (Fig. 2 middle).

## A5. The multifractal index $\alpha$

 $\alpha$  is variously called "the multifractal index", "Levy index of the generator", "degree of multifractality" [Schertzer and Lovejoy, 1987, Schertzer et al., 1997] and its interpretation is more subtle. When H=0,  $\alpha=0$ , and  $C_1>0$ , the process is the turbulent on/off "beta model" and the process is non-zero over a fractal set with codimension  $C_1$ . When  $\alpha=2$  (the maximum), it is a "log-normal" multifractal with fluctuations following log-normal distributions (except for the extremes that have power-law probabilities).

## Appendix B. From fractal sets to multifractal densities: Box, information and correlation fractal dimensions

Strata boundaries define a geometric set of points on the time axis for example, Fig. B1, top. The strongly inhomogeneous nature of the distribution of points is highlighted in Fig. 4 that shows the time intervals  $\tau(n)$  between consecutive ( $n^{th}$  to  $n+1^{th}$ ) boundaries. This was quantified in Fig. 5 that shows probability distribution of  $\tau(n)$  whose "tails" are power laws - scaling in probability space (see below). Other direct demonstrations of the scaling (fractality) of the set of boundary points is given in Fig. B2.

Yet it turns out that rather than the set description that focuses on the relative positions of individual points on the time axis, a more powerful framework is to consider the density  $\rho(t)$  of the points (here, the number per Myr) as the fundamental quantity.  $\rho(t)$  has a value at each point in time, mathematically it is a function, if it is scaling, then in general it is the density of a singular multifractal measure (a "generalized function", like a Dirac function). To go from set to density, we can take the Sepkoski example: Fig. B1 (top) shows the set representation, that was already converted from a set to an indicator function at 1 Myr resolution in Fig. 1 (upper right). From this 1 Myr indicator function, Fig. B1 (second row and below) shows the density representations at various lower resolutions obtained by successively averaging  $\rho(t)$  over factors of four.

The relationship between the fractal set and multifractal density description was clarified in the context of (fractal) strange attractors in deterministic chaos [Grassberger, 1983, Hentschel and Procaccia, 1983]. At the time, several distinct definitions of fractal dimension were in common use; in particular the "box", "information" and "correlation" dimensions  $(D_{box}, D_{inf}, D_{cor})$  respectively). These were shown to be simply part of an infinite (and decreasing) hierarchy of fractal dimensions D(q) with  $D_{box} = D(0)$ ,  $D_{inf} = D(1)$ ,  $D_{cor} = D(2)$ . This hierarchy is determined by the  $q^{th}$  order statistical moments of  $\rho(t)$ ; theoretically,  $D(q) = d - \frac{K(q)}{q-1}$  (see eq. 2, 3) where d is the dimension of the embedding space (here, the time axis, d=1). Note that although mathematically defined fractal sets do have unique Hausdorff dimensions,  $D_{box}$  is often used as a surrogate for real world (finite) sets (yet their mathematical definitions are different).

In terms of the set description,  $D_{box}$ ,  $D_{cor}$  are particularly simple to calculate from point pair statistics; specifically, by considering the average number of points n(L) within a distance L of a given point. For a uniform (nonfractal) distribution in a space of dimension d, the average number  $n_u$  of other points within a distance L from any given point is:  $n_u(L) \approx L^d$ . Since for a uniformly distributed set of points on the time axis, the number in an interval 2L, would be twice as large as in an interval size L, we have:  $n_u(2L) = 2n_u(L)$ ) i.e. d = 1 as expected. In comparison, fractal sets have  $n(L) \approx L^D$  with exponents D < d, but the way the point pairs are chosen is important. One way of choosing point pairs is to take the first point of each pair uniformly at random i.e. not on the fractal set, only the second point is taken on the fractal set. In this case, we obtain the "box dimension"  $D_{box}$ :  $n_{box}(L) \approx L^{D_{box}}$ . Alternatively, we may choose both points in the pair to be from the fractal set itself so that now, the exponent is the correlation dimension:  $n_{cor}(L) \approx L^{D_{cor}}$ . In high dimensional (large d) spaces (e.g. for strange attractors), the set of points on the fractal set may be extremely sparse ( $D \ll d$ ) so that random uniformly chosen points are almost surely far from points on the fractal set, consequently, in high dimensional spaces, the box dimension is numerically inefficient to compute. However, since points on fractal sets are highly clustered, the correlation dimension was also calculated for the set of meteorological measuring stations on the (d = 2) Earth's surface [Lovejoy et al., 1986], where  $D_{cor} = 1.75$ .

In Fig. B2, we applied both box and correlation pair counting methods to the set of boundary points on the time axis (d=1). Whereas n(L) characterizes the frequency of occurrence of the pairs, for the statistics, we are instead interested in the relative frequency, i.e. probabilities. Relative probabilities are obtained from the ratio  $n(L)/n_u(L) \approx L^{D-d} = L^{-C}$  where C = d - D is the codimension and is independent of the embedding space dimension d. Here, the normalization using the uniform number,  $n_u(L)$ , is particularly important because the overall number of points is small, and the dimension (d=1) is low. These combine to imply significant "finite size" effects that are partially cancelled out by using the same algorithm with the same number of points uniformly distributed over the same overall interval to estimate  $n_u(L)$  (here,  $n_u(L)$  was estimated by using a set of points with Gaussian distributed intervals between them). Fig. B2 shows the results for both box counting and correlation analyses where for convenience, the figure displays the inverse ratio  $n_u(L)/n(L) \approx L^C$  with positive exponent C. With the possible exception of the very small (64 point) Graptolite boundaries, the figure shows clear scaling regimes although still with some deviations at both small and large scales. The (rough) codimension estimates are given in Table B1. From the figure and the table, we see that while the box codimensions are roughly zero for the global (GTS, Sepkoski) boundaries, they are nonzero for the zonal ones, and the correlation dimensions are nonzero for all of them.

We can now check that these fractal set descriptions agree with the multifractal density description. This can be done using the above theoretical relation for the density codimension  $C(q) = d \cdot D(q) = K(q)/(q-1)$ . First, consider the correlation dimension with  $C_{cor} = C(2) = K(2)$ . Table B1 shows that these are close to the density estimates from the q=2 trace moments (Fig. 3). It turns out that the q=1 information codimension is not easy to calculate from point pairs and theoretically (since K(1)=0), C(1) must be calculated by taking the limit  $q\to 1$  that yields  $C(1)=K'(1)=C_1$ , (Table B1 gives the estimates of  $C_1$  from trace moments). Finally, taking  $C_1$ 0 yields the box codimension:  $C_2$ 0 yields the universal multifractal model (eq. 2) has  $C_3$ 0 is very poorly estimated empirically (the best way is through the box dimension applied to the set directly as in Fig. B2). Given these theoretical considerations and empirical limitations, we conclude that the set and density based estimates given here are compatible.

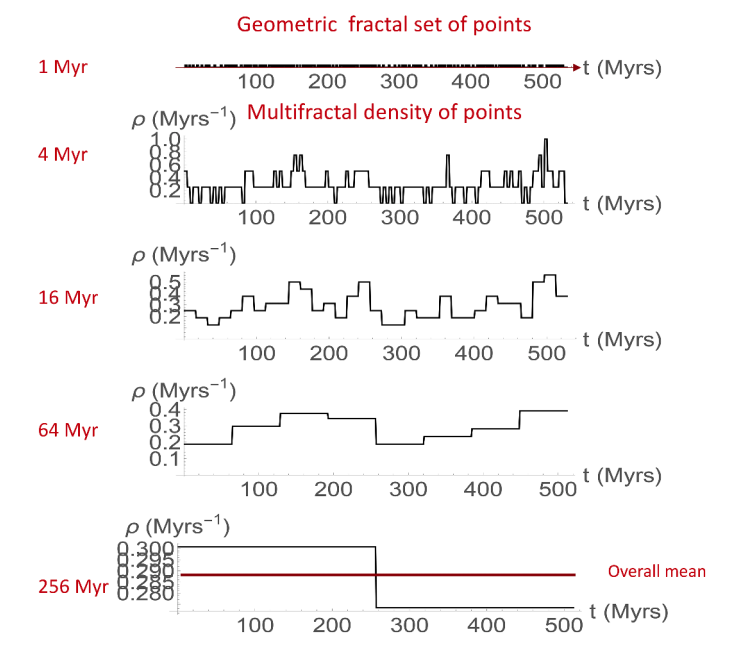


**Fig. B1.** A comparison of the set and density descriptions of the boundaries. An example using the Sepkoski boundaries at 1 Myr resolution. The top represents the boundaries as a fractal set of points on the time axis. At this scale the density of points is the indicator function of the set (shown in Fig. 1 upper right). The lower series shows the boundary densities at lower resolutions, successively degraded by factors of four with the overall mean shown at the bottom in red.

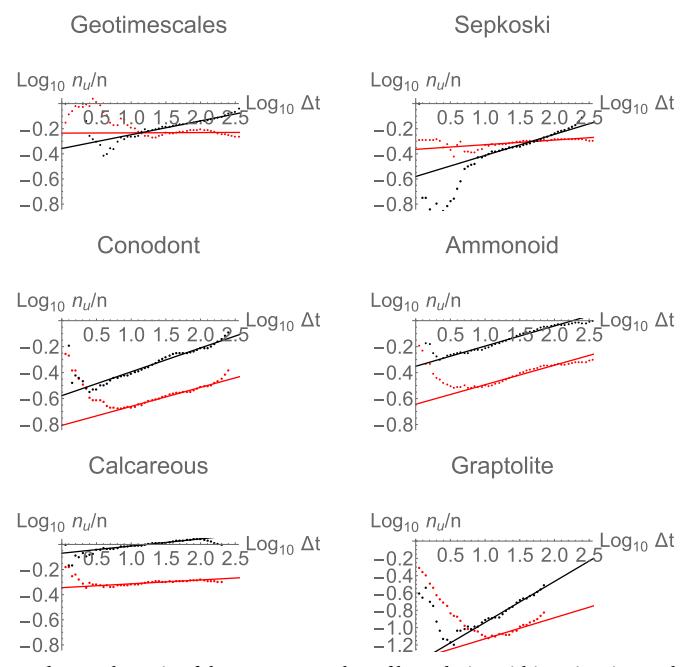


Fig. B2. Box and correlation dimension analyses. The ratio of the average number of boundaries within a time interval  $\Delta t$  (in Myrs) for a uniformly distributed set of boundaries ( $n_u(\Delta t)$ ) to the actual distribution ( $n(\Delta t)$ ). The logarithmic slope is the codimension, the lines show regressions for  $\Delta t > 4$  Myrs; the corresponding fractal dimension is D = 1 - C so that flat (zero slope) lines are nonfractal (D = 1). The black points and lines are  $n_u/n_{cor}$  whose logarithmic slopes are the correlation codimensions and the red points and lines are  $n_u/n_{box}$  whose logarithmic slopes are box codimensions. The values from the slopes are given in Table B1 that also compare these direct correlation dimension estimates with those from the q = 2 trace moment K(2) (=  $C_{cor}$ ), they show generally good agreement. At small and large lags there will be deviations due respectively to chronology errors and to the finite length of the series.

#### Table B1

A comparison of various codimensions. The parameters  $C_1$ , C(2) = K(2) estimated from the (multifractal) density analysis (trace moments, Fig. 3) compared with fractal set analyses ( $C_{box}$ ,  $C_{cor}$ ), Fig. B2. Theoretically, the scaling exponent of the second moment of the point density, K(2) (column 3) should equal the pointwise correlation dimension  $C_{cor}$ , (column 4), a relationship that is reasonably respected (the exception is the Graptolite series that has very few boundaries – 64 - and hence poor statistics). The correlation and box dimensions were estimated as described in the text, from point pairs statistics (Fig. B2). Recall that the fractal dimension D of these sets (embedded on the time axis) is equal to 1- C. Note that for the two global series without missing strata,  $C_{box} \approx 0$  so that they would be nonfractal (or only marginally fractal) if the box dimension was used, yet the correlation dimension shows convincingly that  $C_{cor}>0$  and hence that they are fractal.

| Series                          | $C_1 = (C_{inf})$ | C(2)=K(2) | $C_{cor}$ | $C_{box}$ |
|---------------------------------|-------------------|-----------|-----------|-----------|
| Geotimescales (GTS2020) (1 Myr) | 0.11              | 0.12      | 0.11      | 0.00      |
| Sepkoski sub-stages (1 Myr)     | 0.12              | 0.12      | 0.12      | 0.03      |
| Conodont                        | 0.12              | 0.15      | 0.16      | 0.14      |
| Ammonoid                        | 0.09              | 0.12      | 0.15      | 0.15      |
| Calcareous                      | 0.09              | 0.11      | 0.07      | 0.03      |
| Graptolite                      | 0.15              | 0.18      | 0.44      | 0.24      |

## Appendix C. Compound Multifractal - Poisson Processes (CMPP)

We discussed the fact that the geological time is based on a series of events that may be considered either as a geometrical set of points on the time axis or alternatively as a temporal density of points. In scaling systems these alternatives correspond respectively to fractal sets or to multifractal measures; in appendix B, we provided quantitative links between the two. In all cases, systematic scaling analyses were applied over as wide a range of scales as possible, yet unsurprisingly, to obtain robust statistics of event densities, we saw that the time scales must be long enough so that the granular (black/white) nature of set is no longer important. Indeed, dimensional analysis gives a characteristic time of  $1/\bar{p}$  ( $\approx$  1Myr for the zonal and  $\approx$  3 Myrs for the global series, see Table 1), with shorter time intervals typically having either 0 or 1 events and longer times typically having several events. While this does indeed lead to a small scale/large scale break at around  $\Delta t_c = 1/\bar{p}$  (see e.g. fig. 2), this does not necessarily imply the existence of a corresponding underlying *physical* time scale. Indeed, if the processes generating the events are scaling, then as the resolution is increased, more and events will be observed. This is because there may be more than a unique event in a single resolution element so that as the resolution increases,  $\Delta t_c$  will be shorter and shorter.  $\Delta t_c$  is therefore not a characteristic of the process, but rather of the resolution at which is observed.

$$Pr(N(\Delta t) = \mathcal{N}) = \frac{\prod (\Delta t)^{\mathcal{N}}}{\mathcal{N}!} e^{-\prod (\Delta t)}$$
(8)

(see e.g. [Feller, 1971]). The average event density is thus:

$$\rho_{\Delta t} = \frac{N(\Delta t)}{\Delta t} \tag{9}$$

Certain statistical properties of  $\rho_{\Delta t}$  can easily be determined. For example, standard results for the first and second moments of a Poisson processes are:

$$\overline{N(\Delta t)} = \prod (\Delta t); \quad \overline{N(\Delta t)^2} = \prod (\Delta t) + \prod^2 (\Delta t)$$
(10)

(the overbar indicates Poisson process averaging only). In this compound process, the probability  $\prod(\Delta t)$  is determined from realizations of a multifractal process developed over a range from large (outer) time scale  $\tau_0$  to small (inner, resolution) time scale  $\tau_i$ , with the observing time scale  $\Delta t$  satisfying  $\tau_i \leq \Delta t \leq \tau_0$  (equivalently, with scale ratio  $\lambda = \tau_i / \Delta t$ ) and with the overall average probability density (i.e. with  $\Delta t = \tau_0$ )  $p_{\tau_0} = f < 1$ . Averaging over the multifractality (indicated by "< >"), we find:

$$\langle \overline{\rho_{\Delta t}} \rangle = \frac{\langle \overline{N(\Delta t)} \rangle}{\Delta t} = \frac{\langle \overline{M(\Delta t)} \rangle}{\Delta t} = \langle p_{\Delta t} \rangle = f$$
 (11)

(this follows since  $\langle \prod(\Delta t)\rangle = \Delta t \langle p_{\Delta t}\rangle$  and  $\langle p_{\Delta t}\rangle = f$ , recall K(1)=0, eq. 2, and that multifractal processes are statistically stationary). The time scale quoted above corresponds to the critical time scale  $\Delta t_c$  at which on average there occurs a single event, i.e.  $\langle \overline{N(\Delta t)}\rangle = f\Delta t_c\approx 1$ , i.e.  $\Delta t_c\approx 1$  /f. For example, for the zonal series with nominal resolution 100 kyrs, Table B1 indicates that  $\langle \overline{\rho_{\Delta t}}\rangle \approx 0.1$  per 100 kyr, hence on average, one tenth of the 100 kyr resolution elements have an event, f=0.1 and therefore  $\Delta t_c\approx 1$  Myr. However, the subordinating multifractal process implies a hierarchy of clustering; if we are interested in these large  $\rho$ , p regions, we must consider higher order statistical moments. Using  $\langle p_{\Delta t}\rangle = f$  we have normalized second moments:

$$\frac{\left\langle \overline{\rho_{\Delta t}^2} \right\rangle}{\left\langle \overline{\rho_{\Delta t}} \right\rangle^2} = \left( f \Delta t \right)^{-1} + \frac{\left\langle p_{\Delta t}^2 \right\rangle}{\left\langle p_{\Delta t} \right\rangle^2} = \left( f \Delta t \right)^{-1} + \left( \frac{\Delta t}{\tau_o} \right)^{-K(2)} \tag{12}$$

(see eq. 10, essentially the same result was derived in [Lovejoy and Schertzer, 2006]).  $\langle \overline{\rho_{\Delta t}^2} \rangle / \langle \overline{\rho_{\Delta t}} \rangle^2$  is thus a mixture of power laws. At short intervals, this CPMP second moment differs from the subordinating multifractal moment  $\langle p_{\Delta t}^2 \rangle / \langle p_{\Delta t} \rangle^2$ . Assuming K(2) < 1 the  $(f\Delta t)^{-1}$  term dominates over the (second) multifractal term. Comparing the terms at scale  $\Delta t_c = 1/f$ , we find:

$$\frac{\langle p_{\Delta t}^2 \rangle}{\langle p_{\Delta t} \rangle^2} = N_o^{K(2)}; \quad N_o = f \tau_o \tag{13}$$

where  $N_o$  is the mean number of events over the entire process (up to the outer scale  $\tau_o$ ). For the parameter ranges of interest  $N_o>1$ . For example, taking,  $N_o\approx 100$  and  $K(2)\approx 0.15$  (zonal series, Table B1), we find  $N_o^{K(2)}\approx 2$  so that at  $\Delta t_c$ ,  $\langle \overline{\rho_{\Delta t}^2}\rangle/\langle \overline{\rho_{\Delta t}}\rangle^2$  is already (somewhat) dominated by the multifractal  $\langle p_{\Delta t}^2\rangle/\langle p_{\Delta t}\rangle^2$  term.

Simple formulae for the integer order moments are possible using the Poisson moment generating function, but for the fractional order moments  $\leq 2$  while no analytic results appear to exist, it is simple enough to produce stochastic realizations with the parameters estimated from the scaling (long time) part of the empirical event densities. A full analysis of the CMPP will be made elsewhere. One way of using the model to help interpret the empirical  $\rho(t)$  statistics, is to use the long-time scaling behaviour of  $\rho(t)$  to estimate the parameters of the underlying multifractal process p(t). To roughly reproduce the empirical zonal series (chosen for their higher resolution and larger number of realizations), we made 6 CMPP realizations all with parameters f=0.07,  $C_1=0.1$ ,  $\alpha=1.35$ , (hence K(2)=0.156), and  $\tau_i=0.1$  Myr,  $\tau_0=409.6$  Myrs, so that we have  $\Delta t_c\approx 1.5$  Myrs which is roughly the transition observed (e.g. in fig. 2). Fig. C1 shows the simulations with p(t) in red, p(t) in black, the six simulations are statistically identical, only the random seed is different. Note that occasionally there are spikes in p(t) that lead to multiple Poisson events that would be observed as a single event (the resolution Sadler effect); the Poisson process was therefore truncated to 1 event at the finest simulated resolution (here corresponding to 100 kyrs). This truncation affects the higher order multifractal singularities, not the lower order ones of interest here.

In figs. C2 - 6, we see that the CMPP reproduces the observed statistics very well. Even though it has only two basic ( $C_1$ ,  $\alpha$ ) and three auxiliary parameters ( $\tau_i$ ,  $\tau_o$ , f,) it reproduces the Haar fluctuations (compare fig. C2 with fig. 2), the trace moments (fig. C3 with fig. 3), the time intervals between events (fig. C4 with fig. 4) and probability gap distributions (fig. C5 with fig. 5, the length Sadler effect) and extended Self-Similarity analysis (fig. C6 with fig. 6).

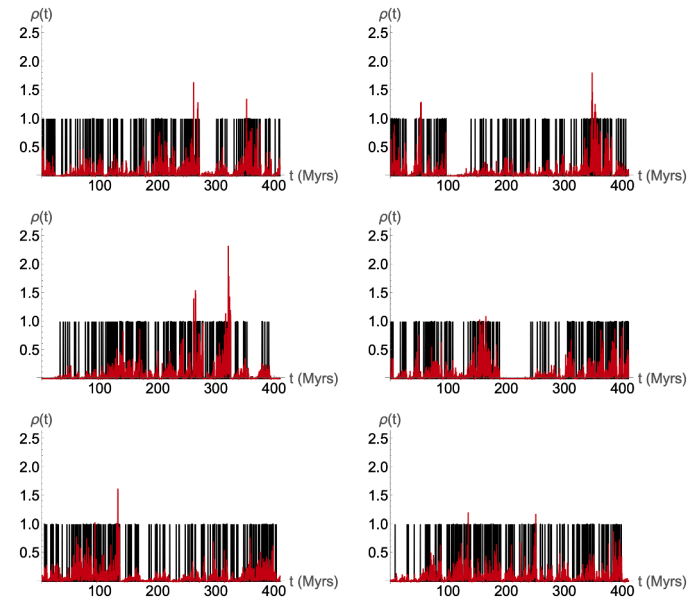
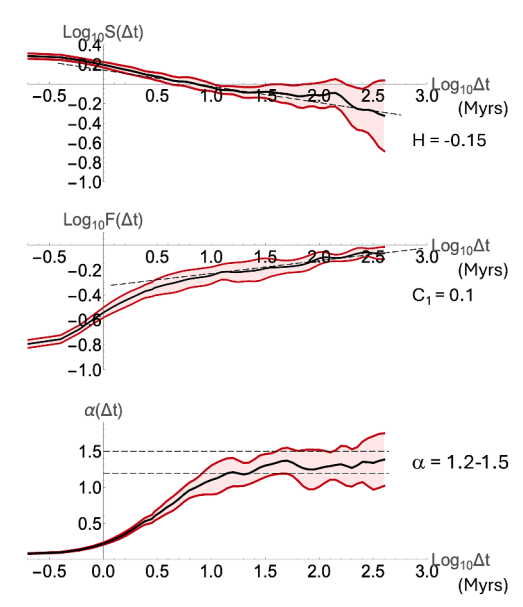


Fig. C1. Six CMPP realizations Temporal boundary event probabilities ( $\rho(t)$ , red) and event densities ( $\rho(t)$ , black). The resolution of the simulations was 100 kyrs with outer scale  $2^{12}$  time longer (409.6 Myrs), the other parameters as indicated in the text. The only difference between the plots is the random seed. The number of boundaries are not identical but close: 257  $\pm$  9. Compare this with fig. 1.



**Fig. C2. Scaling and universal multifractal parameters** H, C<sub>1</sub>, α. Compare this with the empirical fig. 2. The same as the empirical (fig. 2) plots but for the average of 6 realizations of the compound Poisson multifractal model, with resolution 100 kyrs over 12 octaves in scale so that the largest scale is 409.6 Myrs. The mean number of boundaries was 0.5 per Myr, the parameters of the subordinating multifractal process was α = 1.35, C<sub>1</sub> = 0.1, H = 0. There were no other parameters. The realizations are those shown in fig. C1. The compound multifractal-Poisson process is perfectly scale invariant, but there is an implicit scale equal to the inverse of the mean boundary density, and this leads to departures from power law scaling at around 1 - 2 Myr.

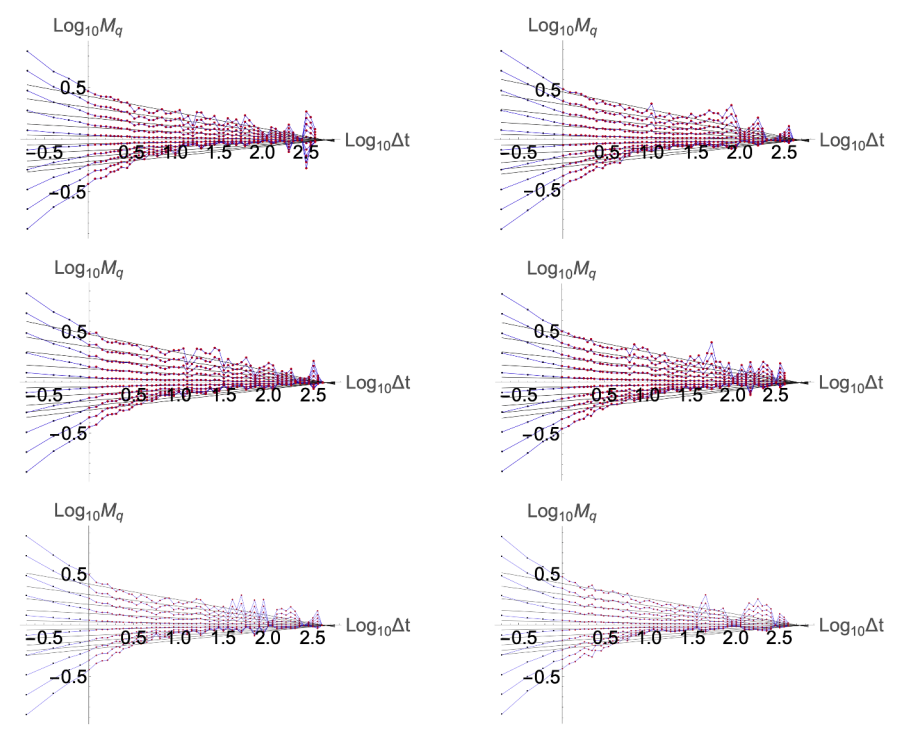


Fig. C3. Trace moments  $M_q = \langle \varphi_{\lambda}^q \rangle$  of the same 6 realizations. With  $\lambda = \tau_0/\Delta t$  and  $\Delta t$  in units of Myrs. Compare this with fig. 3.

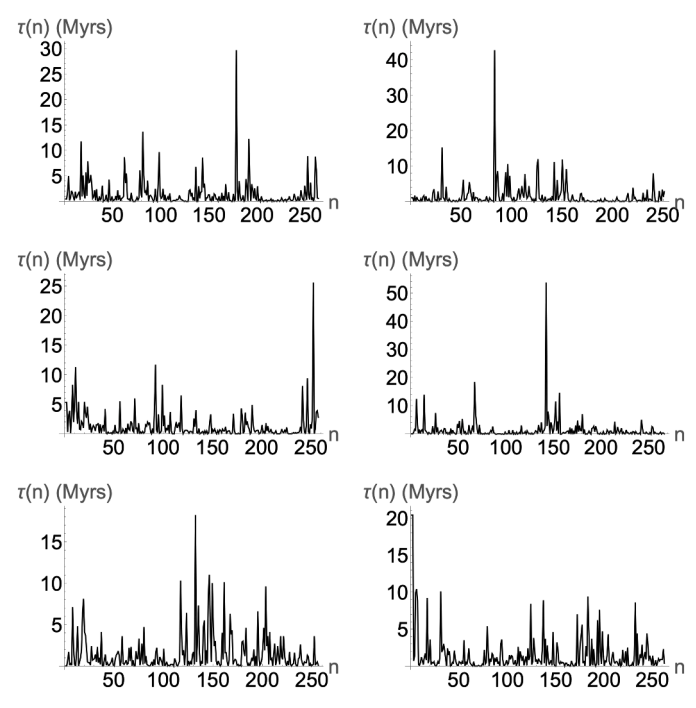


Fig. C4. The  $n^{\text{th}}$  time intervals between successive boundaries  $(\tau(n))$  in Myrs. Compare this with the empirical fig 4.

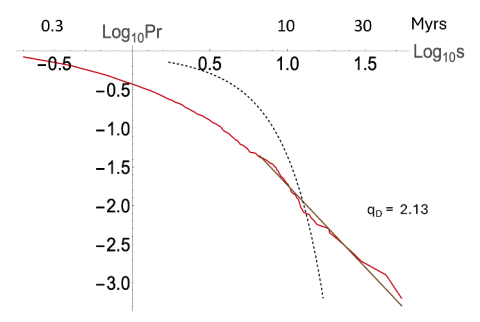


Fig. C5. Probability distributions  $Pr(\tau'>\tau)$  for the duration of a randomly chosen inter-boundary interval  $\tau'>$  exceeding a fixed threshold  $\tau$ . The dashed line is the best fitting Gaussian,  $q_D$  is the absolute slope. Compare this to fig. 5.

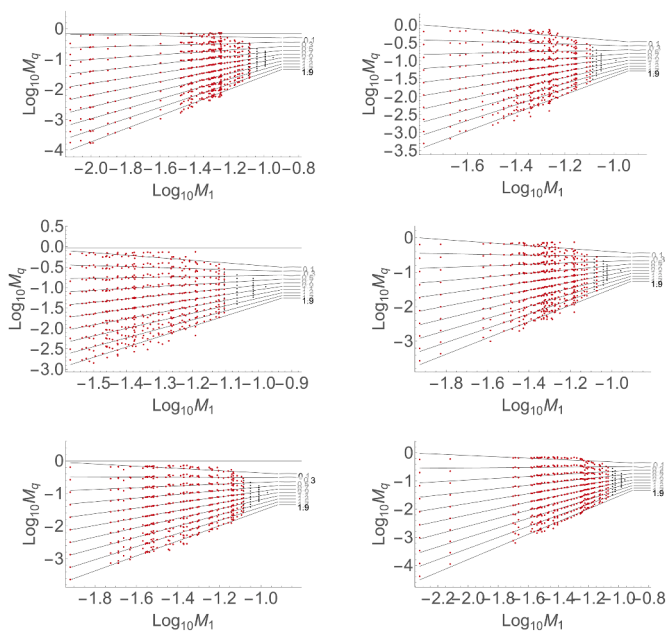


Fig. C6. The extended self-similarity (ESS) plots. The scaling of the  $q^{\text{th}}$  order moments ( $S_q = \log \langle \Delta \rho(\Delta t)^q \rangle = M_q$ ) as functions of the first order moments ( $M_1 = S_1$ ) for moments order q = 0.1, 0.3, ... 1.9 (top to bottom). The regression slopes (= 1 - K(q)/H) are shown indicating the excellent scaling from  $\Delta t \geq 1$  Myr (red points). The fits are over the red points that correspond to lags ( $\Delta t$ )  $\geq 1$  Myr (the black are for  $\Delta t < 1$  Myr). Compare this to fig. 6.

## Data availability

The data are publically available from the references cited in the text.

#### References

- Aretz, M., Herbig, H.G., Wang, X.D., Gradstein, F.M., Agterberg, F.P., Ogg, J.G., 2020. The carboniferous period. In: Gradstein, F.M., Ogg, G., Schmitz, M.D., Ogg, G.M. (Eds.), Geologic Time Scale 2020. Elsevier, pp. 811–874.
- Bapst, D.W, Bullock, P.C., Melchin, M.J., Sheets, H., David, Mitchell, C.E., 2012. Graptoloid diversity and disparity became decoupled during the Ordovician mass extinction. Proceed. Natl. Acad. Sci. 109 (9), 3428–3433.
- Becker, R.T., Marshall, J.E.A., Da Silva, A.-C., Agterberg, F.P., Gradstein, F.M., Ogg, J.G., O. G. M, 2020. The devonian period. In: Gradstein, F.M., Ogg James, G., Schmitz Mark, D. (Eds.), Geologic Time Scale 2020. Elsevier, pp. 733–810.
- Benzi, R., Ciliberto, S., Tripiccione, R., Baudet, C., Massaioli, F., Succi, S., 1993. Extended self-similarity in turbulent flows. Phys. Rev. E 48 (1), R29–R32. https://doi.org/ 10.1103/PhysRevE.48.R29.
- Crampton, J.S., Cooper, R.A., Sadler, P.M., Foote, M., 2016. Greenhouse icehouse transition in the Late Ordovician marks a step change in extinction regime in the marine plankton. Proceed. Natl. Acad. Sci. 113 (6), 1498–1503.
- Crampton, J.S., Meyers, S.R., Cooper, R.A., Sadler, P.M., Foote, M., Harte, D., 2018.

  Pacing of paleozoic macroevolutionary rates by Milankovitch grand cycles.

  Proceedings of the National Academy of Sciences 115 (22), 5686–5691.
- Daumantas, L., Spiridonov, A., 2024. "hespdiv": an R package for spatially constrained, hierarchical, and contiguous regionalization in palaeobiogeography. Palaeontology. –(–), in press.
- Edwards, L.E., 1984. Insights on why graphic correlation (Shaw's method) works. J. Geol. 583–597.
- Edwards, L.E., 1989. Supplemented graphic correlation: a powerful tool for paleontologists and nonpaleontologists. Palaios 127–143.
- Fan, J.-x., Shen, S.-z., Erwin, D.H., Sadler, P.M., MacLeod, N., Cheng, Q.-m., Hou, X.-d., Yang, J., Wang, X.-d., Wang, Y., 2020. A high-resolution summary of cambrian to early triassic marine invertebrate biodiversity. Science 367 (6475), 272–277.
- Feller, W., 1971. An Introduction to probability theory and its applications, vol. 2. Wiley, p. 669.
- Fenton, I.S., Pearson, P.N., Dunkley Jones, T., Farnsworth, A., Lunt, D.J., Markwick, P., Purvis, A., 2016. The impact of cenozoic cooling on assemblage diversity in planktonic foraminifera. Philosoph. Transact. Roy. Soc. B: Biolog. Sci. 371 (1691), 20150224.
- Foote, M., 2005. Pulsed origination and extinction in the marine realm. Paleobiology 40 (2), 6–20.
- Foote, M., 2023. Diversity-dependent diversification in the history of marine animals. Am. Nat. 201 (5), 680–693.
- Gale, A.S., Mutterlose, J., Batenburg, S., Gradstein, F.M., Agterberg, F.P., Ogg, J.G., Petrizzo, M.R., Gradstein, F.M., 2020. The cretaceous period. In: Ogg, G., Schmitz, M.D., Ogg, G.M. (Eds.), Geologic Time Scale 2020. Elsevier, pp. 1023–1086.
- Goldman, D., Sadler, P., Leslie, S.A., O. G. M., 2020. The ordovician period. In: Gradstein Felix, M., Ogg James, G., Schmitz Mark, D. (Eds.), Geologic Time Scale 2020. Elsevier, pp. 631–694.
- Elsevier, pp. 631–694. Gradstein, F.M., 2020. Introduction. In: Gradstein Felix M, O.J.G., Schmitz Mark, D., Ogg Gabi, M. (Eds.), Geologic Time Scale 2020. Elsevier, pp. 3–20.
- Grassberger, P., 1983. Generalized dimensions of strange attractors. Physical Review Letter, A 97, 227.
- Henderson, C.M., Shen, S.Z., Gradstein, F.M., Agterberg, F.P., 2020. The permian period. In: Gradstein, F.M., Ogg, G., Schmitz, M.D., Ogg, G.M. (Eds.), Geologic Time Scale 2020. Elsevier, pp. 875–902.
- Hentschel, H.G.E., Procaccia, I., 1983. The infinite number of generalized dimensions of fractals and strange attractors. Physica D 8, 435–444.
- Hesselbo, S.P., Ogg, J.G., Ruhl, M., Hinnov, L.A., Huang, C.J., 2020. The Jurassic period. In: Gradstein, F.M., Ogg, G., Schmitz, M.D., Ogg, G.M. (Eds.), Geologic Time Scale 2020. Elsevier, pp. 955–1021.
- Hinnov, L.A., Ogg, J.G., 2007. Cyclostratigraphy and the astronomical time scale. Stratigraphy 4 (2–3), 239–251.
- Hinnov, L.A., 2018. Cyclostratigraphy and astrochronology in 2018. Stratigraphy & Timescales. Elsevier, pp. 1–80.
- Korvin, G., Boyd, D.M., O'Dowd, R., 1990. Fractal characterization of the South Australian gravity station network. Geophys. J. Int. 100 (3), 535–539.
- Lieberman, B.S., Melott, A.L., 2013. Declining volatility, a general property of disparate systems: from fossils, to stocks, to the stars. Palaeontology 56 (6), 1297–1304.
- Lovejoy, S., D. Schertzer, 2006: Stereophotography of rain drops and compound poisson-cascade processes, Proceedings, American Meteor. Soc. Cloud conference, Madison, July 12-14, p. 14.4.1-14.4.19. https://www.physics.mcgill.ca/~gang/eprints/eprint Lovejoy/neweprint/AMS.drop.26.5.6.pd.
- Lovejoy, S., Schertzer, D., 2012. Haar wavelets, fluctuations and structure functions: convenient choices for geophysics. Nonlinear Proc. Geophys. 19, 1–14. https://doi. org/10.5194/npg-19-1-2012.
- Lovejoy, S., Schertzer, D., 2013. The Weather and Climate: Emergent Laws and Multifractal Cascades. Cambridge University Press, p. 496.

- Lovejoy, S., Spiridonov, A., 2024. The Fractional Macroevolution Model, a simple quantitative macroevolution model. Paleobiology 1–25. https://doi.org/10.1017/ pab.2023.38.
- Lovejoy, S., Schertzer, D., Ladoy, P., 1986. Fractal characterisation of inhomogeneous measuring networks. Nature 319, 43–44.
- Lovejoy, S., Davies, R., Spiridonov, A., Hebert, R., Lambert, F., 2025. Time scales and gaps: Haar Fluctuations and multifractal Geochronologies. submitted to Earth and Plan. Sci. Lett.
- Lovejoy, S., 2013. What is climate? Eos (Washington DC) 94 (1), 1-2,, 1 January.
- Lovejoy, S., 2015. A voyage through scales, a missing quadrillion and why the climate is not what you expect. Clim. Dyn. 44, 3187–3210. https://doi.org/10.1007/s00382-014-2324-0
- Lovejoy, S., 2018. The spectra, intermittency and extremes of weather, macroweather and climate. Nat. Sci. Rep. 8, 1–13. https://doi.org/10.1038/s41598-018-30829-4.
- Lovejoy, S., 2023. Scaling, dynamical regimes and stratification: how long does weather last? How big is a cloud? Nonlin. Process Geophys. 30, 311–374. https://doi.org/10.5194/npg-30-311-2023.
- Mandelbrot, B.B., 1974. Intermittent turbulence in self-similar cascades: divergence of high moments and dimension of the carrier. J Fluid Mech 62, 331–350.
- Marwan, N., Thiel, M., Nowaczyk, N.R., 2002. Cross recurrence plot based synchronization of time series. Nonlin. Process Geophys. 9 (3/4), 325–331.
- Melchin, M.J., Sadler, P.M., Cramer, B.D., 2012. The silurian period. In: Gradstein, F.M., Ogg, J.G., Schmitz, M. (Eds.), The Geologic Time Scale2012, 2-volume Set. Elsevier, pp. 525–558.
- Melchin, M.J., Sadler, P.M., Cramer, B.D., 2020. The silurian period. Geologic Time Scale 2020. Elsevier, pp. 695–732.
- Nicolis, C., 1993. Optimizing the global observational network a dynamical-approach. J. Appl. Meteor. 32, 1751–1759.
- Ogg, J.G., Chen, Z.-Q., Orchard, M.J., Jiang, H.S., 2020. The triassic period. In: Gradstein, F.M., Ogg, G., Schmitz, M.D., Ogg, G.M. (Eds.), Geologic Time Scale 2020. Elsevier, pp. 903–953.
- Parisi, G., Frisch, U., 1985. A multifractal model of intermittency. In: Ghil, M., Benzi, R., Parisi, G. (Eds.), Turbulence and predictability in geophysical fluid dynamics and climate dynamics. North Holland, pp. 84–88.
- Peng, S.C., Babcock, L.E., Ahlberg, P., 2020. Chapter 19—The cambrian period. In: Gradstein, F.M., Ogg, J.G., Schmitz, M.D., Ogg, G.M. (Eds.), Geologic Time Scale. Elsevier.
- Puolamäki, K., Fortelius, M., Mannila, H., 2006. Seriation in paleontological data using Markov Chain Monte Carlo methods. PLoS Comput. Biol. 2 (2), e6.
- Radzevičius, S., Spiridonov, A., Brazauskas, A., 2014. Application of wavelets to the cyclostratigraphy of the upper homerian (Silurian) Gėluva regional stage in the Viduklė-61 deep well (Western Lithuania). In: Pais, J. (Ed.), STRATI 2013. Springer, pp. 437–440.
- Raffi, I., et al., 2020. The neogene period. In: Gradstein, F.M., Ogg, G., Schmitz, M.D., Ogg, G.M. (Eds.), Geologic Time Scale 2020. Elsevier, pp. 1141–1215.
- Raup, D., Sepkoski, J., 1982. Mass extinctions in the marine fossil record. Science 215 (4539), 1501–1503.
- Sadler, P.M., Kemple, W.G., Kooser, M.A., 2003. CONOP9 programs for solving the stratigraphic correlation and seriation problems as constrained optimization. High Resolution Approaches in Stratigraphic Paleontology. Kluwer Academic Publishers, Boston, pp. 461–465. Springer.
- Sadler, P.M., Cooper, R.A., Crampton, J.S., 2014. High-resolution geobiologic time-lines: progress and potential, fifty years after the advent of graphic correlation. Sediment. Record. 12 (3), 4–9.
- Sadler, P.M., 1981. Sediment accumulation rates and the completeness of stratigraphic sections. J. Geol. 89 (5), 569–584.
- Sadler, P.M., 2004. Quantitative biostratigraphy-achieving finer resolution in global correlation. Annu. Rev. Earth Planet. Sci. 32, 187–213.
- Schertzer, D., Lovejoy, S., 1983. On the dimension of atmospheric motions. In: paper presented at IUTAM Symp. on turbulence and chaotic phenomena in fluids. Kyoto, Japan.
- Schertzer, D., Lovejoy, S., 1987. Physical modeling and analysis of rain and clouds by anisotropic scaling of multiplicative processes. J. Geophys. Res. 92, 9693–9714.
- Schertzer, D., Lovejoy, S., 1987. Physical modeling and Analysis of Rain and Clouds by Anisotropic Scaling of Multiplicative Processes. Journal of Geophysical Research 92, 9693–9714.
- Schertzer, D., Lovejoy, S., Schmitt, F., Chigirinskaya, Y., Marsan, D., 1997. Multifractal cascade dynamics and turbulent intermittency. Fractals 5, 427–471.
- Sepkoski Jr., J.J., 2002. A compendium of fossil marine animal genera. Bull. Am. Paleontol. 363, 1–560.
- Shaw, A.B., 1964. Time in Stratigraphy. McGraw-Hill Book Company, p. 365.
- Speijer, R.P., Pälike, H., Hollis, C.J., Hooker, J.J., Ogg, J.G., 2020. The paleogene period. In: Gradstein, F.M., Ogg, G., Schmitz, M.D., Ogg, G.M. (Eds.), Geologic Time Scale 2020. Elsevier, pp. 1087–1140.
- Spiridonov, A., Lovejoy, S., 2022. Life rather than climate influences diversity at scales greater than 40 million years. Nature 607, 307–312. https://doi.org/10.1038/ s41586-022-04867-v.
- Spiridonov, A., Brazauskas, A., Radzevičius, S., 2016. Dynamics of abundance of the midto late Pridoli conodonts from the eastern part of the Silurian Baltic Basin: multifractals, state shifts, and oscillations. Am. J. Sci. 316 (4), 363–400. https://doi. org/10.2475/04.2016.03.

- Spiridonov, A., Samsonė, J., Brazauskas, A., Stankevič, R., Meidla, T., Ainsaar, L., Radzevičius, S., 2020a. Quantifying the community turnover of the uppermost Wenlock and Ludlow (Silurian) conodonts in the Baltic Basin. Palaeogeogr. Palaeoclimatol. Palaeoecol. 549, 109128.
- Spiridonov, A., et al., 2020b. Ultra-high resolution multivariate record and multiscale causal analysis of Pridoli (late Silurian): implications for global stratigraphy, turnover events, and climate-biota interactions. Gondwan. Res. 86, 222–249. https://doi.org/10.1016/j.gr.2020.05.015.
- Spiridonov, A., Balakauskas, L., Lovejoy, S., 2022. Longitudinal expansion fitness of brachiopod genera controlled by the Wilson cycle. Glob. Planet. Change 216.
   Spiridonov, A., 2017. Recurrence and cross Recurrence plots reveal the onset of the Mulde event (Silurian) in the abundance data for Baltic conodonts. J. Geol. 125 (3), 221 202
- Stern, R.J., 2023. The orosirian (1800–2050 Ma) plate tectonic episode: key for reconstructing the proterozoic tectonic record. Geosci. Front. 14 (3), 101553.
  Tessier, Y., Lovejoy, S., Schertzer, D., 1994. The multifractal global raingage network: analysis and simulation. J. Appl. Meteorol. 32 (12), 1572–1586.